

A complete model of CH⁺ rotational excitation including radiative and chemical pumping processes

B. Godard¹ and J. Cernicharo¹

Departamento de Astrofísica, Centro de Astrobiología, CSIC-INTA, Torrejón de Ardoz, Madrid, Spain

Received 2 August 2012 / Accepted 5 November 2012

Abstract

Aims. Excitation of far-infrared and submillimetric molecular lines may originate from nonreactive collisions, chemical formation, or far infrared, near-infrared, and optical fluorescences. As a template, we investigate the impact of each of these processes on the excitation of the methylidyne cation CH⁺ and on the intensities of its rotational transitions recently detected in emission in dense photodissociation regions (PDRs) and in planetary nebulae.

Methods. We have developed a nonlocal thermodynamic equilibrium (non-LTE) excitation model that includes the entire energy structure of CH⁺, i.e. taking into account the pumping of its vibrational and bound and unbound electronic states by near-infrared and optical photons. The model includes the theoretical cross-sections of nonreactive collisions with H, H₂, He, and e⁻, and a Boltzmann distribution is used to describe the probability of populating the excited levels of CH⁺ during its chemical formation by hydrogenation of C⁺. To confirm our results we also performed an extensive analytical study, which we use to predict the main excitation process of several diatomic molecules, namely HF, HCl, SiO, CS, and CO.

Results. At densities $n_{\text{H}} = 10^4 \text{ cm}^{-3}$, the excitation of the rotational levels of CH⁺ is dominated by the radiative pumping of its electronic, vibrational, and rotational states if the intensities of the radiation field at ~ 0.4 , ~ 4 , and $\sim 300 \mu\text{m}$ are stronger than 10^5 , 10^8 , and 10^4 times those of the local interstellar radiation field (ISRF). Below these values, the chemical pumping is the dominant source of excitation of the $J > 1$ levels, even at high kinetic temperatures ($\sim 1000 \text{ K}$). The far-infrared emission lines of CH⁺ observed in the Orion Bar and the NGC 7027 PDRs are consistent with the predictions of our excitation model assuming an incident far-ultraviolet (FUV) radiation field of $\sim 3 \times 10^4$ (in Draine's unit) and densities of $\sim 5 \times 10^4$ and $\sim 2 \times 10^5 \text{ cm}^{-3}$. In the case of NGC 7027, the estimate of the density is 10 to 100 times lower than those deduced by traditional excitation codes. Applying our model to other X¹Σ⁺ ground state diatomic molecules, we find that HF, and SiO and HCl are the species the most sensitive to the radiative pumping of their vibrational and bound electronic states. In both cases, the minimal near-infrared and optical/UV radiation field intensities required to modify their rotational level populations are $\sim 10^3$ times those of the local ISRF at densities $n_{\text{H}} = 10^4 \text{ cm}^{-3}$. All these results point towards interstellar media with densities lower than previously established and cast doubts on the clumpiness of well-studied molecular clouds.

Key words. Line formation - molecular processes - radiative transfer - ISM: molecules

1. Introduction

Our knowledge of the physical conditions of interstellar and circumstellar molecular clouds has grown through the confrontation of the observed intensities and shapes of atomic and molecular lines with those predicted by radiative transfer models. The puzzle consists of simultaneously reproducing the emission profiles of various species observed in a single astronomical source with the minimal number of physical components with different temperatures, densities, and velocity fields. However, the reliability of the results strongly depends on the approximations of the radiative transfer models, and in particular, on the processes expected to drive the distribution of a molecule among its excited levels. For instance, Morris (1975) and Carroll & Goldsmith (1981) have shown that considering only the excitation by nonelastic collisions and the radiative transitions between the rotational levels of the ground vibrational state may lead to an overestimation (by several orders of magnitude) of the density of the main collisional partner or of the column density of the molecule.

Previous theoretical investigations of alternative excitation mechanisms have mainly focused on the capacity of near-infrared photons emitted by polycyclic hydrocarbon molecules

(PAHs) to pump the molecules to an excited vibrational state in bright PDRs (Scoville et al. 1980; Giard et al. 1997). While this mechanism is negligible for certain transitions (e.g. HF (1 – 0) and HCl (1 – 0), Agúndez et al. 2011), the near- and mid-infrared pumping of the vibrational states has been found to dominate the rotational excitation of several other species (e.g. H₂O, HNC, NH₃) in the circumstellar envelopes of AGB stars such as IRC10216 (González-Alfonso & Cernicharo 1999; González-Alfonso et al. 2007; Agúndez et al. 2008). Similarly, the pumping of the electronic states by absorption of UV and optical photons followed by radiative decay has been proposed to play a major role in the rotational excitation of diatomic molecules (Cernicharo et al. 1997). For instance, this process has been studied to account for the near-infrared emission lines of H₂ detected in the interstellar and circumstellar media (e.g. Black & van Dishoeck 1987; Habart et al. 2005), the rovibrational emission lines of CO detected in molecular clouds and circumstellar disks (e.g. Krotkov et al. 1980; Troutman et al. 2011), the rotational fine structure absorption lines of interstellar C₂ (van Dishoeck & Black 1982), the 405 nm band of interstellar C₃ observed in absorption towards HD210121 (Roueff et al. 2002), and the rovibronic emission lines of CH⁺ detected in the blue spectrum of the Red Triangle nebula (Balm & Jura 1992).

Lastly, state-to-state chemistry, i.e. chemical reactions between the specific quantum states of the reagents and the products, may be involved in the excitation of a molecular species if the timescale of the reaction is comparable to that of nonreactive and nonelastic collisions (Black 1998). Indeed, molecular excitation via the chemical formation itself has already been proposed to populate the highest rotational levels of interstellar C₃ (Roueff et al. 2002), and has recently been invoked by Goicoechea et al. (2011) as an alternative solution to explain the extended and intense rotational emission of OH detected in the Orion Bar PDR with the Herschel/PACS instrument.

Because all these processes could alter our concept of many astrophysical environments (from interstellar and circumstellar PDRs to protoplanetary disks), it is essential to methodically explore their respective role on the rotational emission lines of each molecular species. While other diatomic molecules, such as OH and SiO, will be treated in forthcoming papers, we focus here on the methyldyne cation. Since the discovery of CH⁺ in the interstellar medium by Douglas & Herzberg (1941), the energy structure, spectroscopic properties, nonreactive collisional processes, and the chemistry of this molecular ion have been the subject of both experimental and theoretical studies (e.g. Hakalla et al. 2006; Müller 2010; Turpin et al. 2010; Gerlich et al. 1987; Hierl et al. 1997 and reference therein). We have collated this information here into a concise paper with the aim to present a complete model of CH⁺ rotational excitation and propose an interpretation of its far-infrared emission lines recently observed with ISO and the Herschel Space Observatory.

2. Pumping mechanisms of CH⁺

2.1. Energy structure

Table 1. Equilibrium molecular constants (in cm⁻¹) of the two first electronic states of CH⁺ (Hakalla et al. 2006). Numbers in parenthesis are power of 10.

constant	X ¹ Σ ⁺	A ¹ Π
T_e		2.41187262 (+4)
ω_e	2.8575609 (+3)	1.864402 (+3)
$\omega_e x_e$	5.93179 (+1)	1.158317 (+2)
$\omega_e y_e$	2.2534 (-1)	2.6301
B_e	1.41774612 (+1)	1.1886774 (+1)
α_e	4.94739 (-1)	9.1629 (-1)
γ_e	2.4904 (-3)	-2.292 (-2)
ϵ_e		4.952 (-3)
D_e	1.38914 (-3)	1.929606 (-3)
β_e	-2.66 (-5)	1.07331 (-4)
δ_e		-1.3123 (-5)
H_e	1.2036 (-7)	
α_{H_e}	2.079 (-8)	
q_e		4.1018 (-2)
α_{q_e}		-3.135 (-3)
q_{D_e}		-2.2 (-5)

Direct spectroscopic measurements of the pure rotational spectrum of CH⁺ are both chemically and technically difficult to achieve because (a) CH⁺ is an extremely reactive species and thus hard to maintain in detectable amounts, and (b) its rotational transitions lie at submillimeter and far-infrared wavelengths where the sensitivity of laboratory spectrometers has been limited until recently (Pearson & Drouin 2006). Hence,

prior to Pearson & Drouin (2006), who reported the first laboratory detection of the CH⁺ $J = 1 - 0$ line, all CH⁺ spectroscopic data were deduced from the measurements of the rovibronic bands X¹Σ⁺ - A¹Π, ¹Δ - ¹Π, and ³Σ - ³Π (e.g. Carre 1968; Carrington & Ramsay 1982; Hakalla et al. 2006) and from the pure rotational spectrum observed towards NGC 7027 (Cernicharo et al. 1997).

Referring to Fig. 1, which displays the energy structure of the Douglas-Herzberg band system (A¹Π - X¹Σ⁺), the first X¹Σ⁺ and A¹Π electronic states of CH⁺ are split into a set of rovibrational levels. Their respective energies E are described by the direct matrix elements of the effective Hamiltonian (Brown et al. 1979). Taking into account the spin-orbit coupling that results in splitting each rotational level in closed-spaced pairs of opposite parity (e and f levels, Brown et al. 1975), the energies of all levels can be computed as

$$\begin{aligned}
 E(\Lambda, v, J) = & T_e(\Lambda) + \omega_e(\Lambda)(v + \frac{1}{2}) - \omega_e x_e(\Lambda)(v + \frac{1}{2})^2 + \omega_e y_e(\Lambda)(v + \frac{1}{2})^3 + \\
 & \left[B_e(\Lambda) - \alpha_e(\Lambda)(v + \frac{1}{2}) + \gamma_e(\Lambda)(v + \frac{1}{2})^2 + \epsilon_e(\Lambda)(v + \frac{1}{2})^3 \right] \times \\
 & (J(J+1) - \Lambda^2) - \\
 & \left[D_e(\Lambda) + \beta_e(\Lambda)(v + \frac{1}{2}) + \delta_e(\Lambda)(v + \frac{1}{2})^2 \right] (J(J+1) - \Lambda^2)^2 + \\
 & \left[H_e(\Lambda) - \alpha_{H_e}(\Lambda)(v + \frac{1}{2}) \right] (J(J+1) - \Lambda^2)^3 \pm \\
 & \frac{1}{2} \left[q_e(\Lambda) + \alpha_{q_e}(\Lambda)(v + \frac{1}{2}) \right] (J(J+1)) \pm \\
 & \frac{1}{2} q_{D_e}(\Lambda) (J(J+1))^2,
 \end{aligned}$$

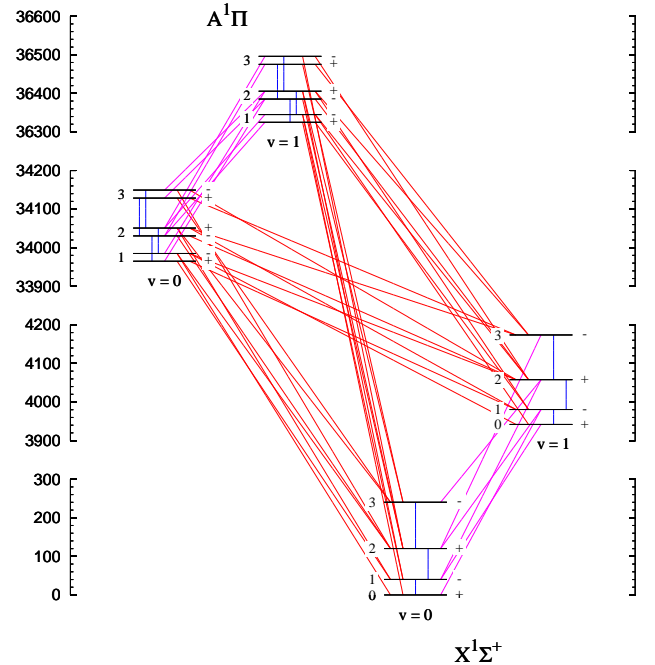


Figure 1. Energies (in K) of the rovibrational levels of the first X¹Σ⁺ and A¹Π electronic states of CH⁺. v -, J -, and P -values are given on the left, below, and on the right of each level. All allowed radiative transitions are displayed, including pure rotational (in blue), rovibronic (in purple), and electronic (in red) transitions.

(1) 2.3. Nonreactive nonelastic collisional processes

where $T_e(\Lambda)$, $\omega_e(\Lambda)$, etc. are the equilibrium molecular constants of the electronic state Λ , and where + and – refer to the e and f sublevels. Each level is therefore defined by its total orbital angular momentum Λ , vibrational momentum ν , total angular momentum J , and parity P . With the equilibrium molecular constants derived by Hakalla et al. (2006) and given in Table 1, the electronic, pure vibrational, and pure rotational level structures of CH⁺ are significantly separated in energy from one another as long as $\nu < 10$ and $J < 13$.

2.2. Nondissociative radiative processes

In astrophysical environments, the level populations of a molecule are controlled by the spontaneous and induced radiative processes and the collisional excitation. As shown in Fig. 1, we consider here all possible radiative transitions of CH⁺ that meet the selection rules $\Delta\Lambda = 0, \pm 1, \Delta S = 0, \Delta J = 0$ (if $\Delta\Lambda \neq 0$), ± 1 , and $P'P'' = -1$. The pure rotational transitions lie in the mid- and far-infrared part of the electromagnetic spectrum from 10 to 1000 μm , the rovibrational lines occupy the near- and mid-infrared domain between 1 and 10 μm , and the rovibronic transitions involve ultraviolet and optical photons between 0.3 and 0.8 μm .

With the conventions adopted by Larsson (1983), the absorption line oscillator strength f and the Einstein spontaneous emission coefficient A of a transition $\Lambda', \nu', J' \rightarrow \Lambda'', \nu'', J''$ of a diatomic molecule are given by

$$f_{\Lambda'\nu'J'\Lambda''\nu''J''} = \frac{8\pi^2 m_e \nu}{3he^2} M_{\Lambda'\nu'J'\Lambda''\nu''}^2 \frac{S_{\Lambda''J''}^{\Lambda'J'}}{2J'' + 1}, \quad (2)$$

and

$$A_{\Lambda'\nu'J'\Lambda''\nu''J''} = \frac{8\pi^2 \nu^2 e^2}{m_e c^3} \frac{2J'' + 1}{2J' + 1} f_{\Lambda'\nu'J'\Lambda''\nu''J''}, \quad (3)$$

where m_e and e are the mass and the charge of the electron, h is the Planck constant, c is the speed of light, and ν , M , and S are the frequency, the transition dipole moment, and the Hönl-London factors (Herzberg 1950). Under the Born-Oppenheimer and the r -centroid approximations, the electronic and nuclear motions are separated and M can be expressed as

$$M_{\Lambda'\nu'J'\Lambda''\nu''}^2 = q_{\Lambda'\nu'J'\Lambda''\nu''} R_e^2(\bar{r}_{\nu'\nu''}), \quad (4)$$

where \bar{r} is the r -centroid of the $\nu' - \nu''$ vibrational band, q is the Franck-Condon factor, and R_e is the electronic transition moment.

Collecting the vibrational band oscillator strengths computed by Elander et al. (1977) and measured by Weselak et al. (2009), and using the Franck-Condon factors and r -centroids obtained by Hakalla et al. (2006), we found that the electronic transition moment of the $A^1\Pi - X^1\Sigma^+$ system has a clearly defined functional form (with a correlation coefficient of 0.97)

$$R_e(\bar{r}_{\nu'\nu''}) = 2.01 \times \exp(-1.66 \bar{r}_{\nu'\nu''}) \quad ea_0. \quad (5)$$

Conversely, since we were unable to extract a simple relation between the transition dipole moment and the internuclear separation (Chackerian & Tipping 1982) for the $X^1\Sigma^+ - X^1\Sigma^+$ system, we extrapolated $M_{0\nu'0\nu''}$ from the values computed at lower ν' by Cheng et al. (2007) and Follmeg et al. (1987) assuming an exponential dependence on $\nu' - \nu''$. Table 2 contains the corresponding Einstein spontaneous emission coefficients computed for the $J', J'' = 1, 0$ transitions of the first vibrational bands of the $A^1\Pi - X^1\Sigma^+$ and $X^1\Sigma^+ - X^1\Sigma^+$ systems.

Since we aim to study the CH⁺ excitation mechanisms over a wide domain of parameters (i.e. describing different astronomical sources), and, for example, at kinetic temperature T_K close to the equivalent temperatures of the rovibrational transitions (> 1000 K), we include all nonreactive collisional excitation and de-excitation processes, even between two different rovibronic levels, and considering H, H₂, He, and e[−] as collision partners. Unfortunately, there are no experimental data available for the CH⁺ collisional rates, and the theoretical data are usually limited to the pure rotational levels.

For collisions with electrons, we adopted the rate functions of T_K obtained by Lim et al. (1999) for $\nu = 0$ and J up to 7. For collisions with neutrals, we used the CH⁺-He collisional rates computed by Hammami et al. (2008, 2009) and Turpin et al. (2010) for $\nu = 0$ and J up to 10, and then applied the rigid rotator approximation¹ to take into account collisions with H and H₂. For $300\text{K} \leq T_K \leq 2000\text{K}$, we used the data of Hammami et al. (2009). Below this temperature range, we preferentially adopted the values computed by Turpin et al. (2010) rather than those of Hammami et al. (2008) because the former authors have found that including of the long-range charge-induced dipole potential of CH⁺ has an impact on the collisional rates at low temperature. Finally, for T_K higher than 2000 K, we extrapolated the de-excitation rates by collisions with neutrals from the values computed at lower temperature assuming a power law dependence on T_K .

These nonreactive collisional rates were used for all transitions with $\Lambda' = \Lambda''$ and $\nu' = \nu''$. In turn, the $\nu' = \nu'' + 1$ collisional rates were deduced from the theoretical cross-sections for inelastic collisions between CH⁺ and He computed by Stoecklin & Voronin (2008) for $\nu', \nu'' = 1, 0$ and J', J'' up to 0, 5. For all other transitions occurring between two different vibrational or electronic levels, the downward rates were inferred from those of the pure rotational transitions assuming a power-law dependence on $(E' - E'')$,

$$k_{\Lambda'\nu'J'\Lambda''\nu''J''}^C = (2J' + 1)(2J'' + 1) \times a \left(\frac{E' - E''}{T_K} \right)^b, \quad (6)$$

where E' and E'' are the energies of the upper and lower levels and a and b are the best-fit coefficients of all available data at the temperature T_K . As a justification for this choice, the obtained scaling relations are found to describe the pure rotational transition rates within a factor of 3 and with a correlation coefficient ranging from 0.8 to 0.9. We note, however, that they systematically underestimate the vibrational transition rates estimated from the cross sections of Stoecklin & Voronin (2008) by a factor varying from 70 to 5 for $10 \leq T_K \leq 70$ K, because the vibrational and rotational quenching cross sections have the same order of magnitude in the low collision energy limit (Stoecklin & Voronin 2008), and by a factor < 5 for $T_K > 70$ K. Nonetheless, since the discrepancies diminish when T_K increases and because our subsequent analysis and predictions will mainly come from the high kinetic temperature domain, we consider our fitting approach as valid.

¹ Within the rigid rotator approximation, the collisional rates are proportional to $\mu^{-1/2}$, where μ is the relative mass of the system collider-CH⁺.

Table 2. Einstein spontaneous emission coefficients $A_{\Lambda v' J' \Lambda'' v'' J''}$ (in s⁻¹) computed for the $J', J'' = 1, 0$ transitions. The data are taken from Hakalla et al. (2006) for the CH⁺ $A^1\Pi - X^1\Sigma^+$ band system (top) and from Cheng et al. (2007) and Follmeg et al. (1987) for the CH⁺ $X^1\Sigma^+ - X^1\Sigma^+$ band system (bottom). Numbers in parenthesis are power of 10.

$A^1\Pi - X^1\Sigma^+$ system					
$v'' \setminus v'$	0	1	2	3	4
0	4.2477 (+05)	2.9239 (+05)	1.4146 (+05)	6.2836 (+04)	2.8210 (+04)
1	7.4827 (+04)	6.3350 (+04)	1.9902 (+05)	1.9663 (+05)	1.4058 (+05)
2	8.6810 (+03)	6.5169 (+04)	1.5824 (+03)	3.7705 (+04)	9.7514 (+04)
3	6.7337 (+02)	1.8585 (+04)	1.9247 (+04)	2.4184 (+04)	1.3421 (+03)
4	4.1285 (+01)	2.7788 (+03)	1.7104 (+04)	1.5654 (+01)	1.2255 (+04)

$X^1\Sigma^+ - X^1\Sigma^+$ system					
$v'' \setminus v'$	0	1	2	3	4
0	6.4002 (-03)	5.6751 (-01)	4.6023 (-04)	1.3972 (-07) ^a	3.0814 (-11) ^a
1		5.7869 (-03)	1.1568 (+00)	5.4871 (-02)	1.1272 (-04) ^a
2			5.2477 (-03)	1.8541 (+00)	6.7870 (-01)
3				4.7379 (-03)	3.0926 (+00)
4					4.2613 (-03)

^a Extrapolated values assuming $M_{0v'00} = 0.65 \times \exp[-4.61 v'] ea_0$, and $M_{0v'01} = 0.50 \times \exp[-3.38 (v' - 1)] ea_0$.

2.4. Reactive collisional processes and photodissociation

Finally, since the chemical timescales of CH⁺ are comparable with those of the nonreactive nonelastic collisions (Bruderer et al. 2010), we took into account the excitation and de-excitation of CH⁺ during its chemical formation and destruction.

During the past decades, the advances of the cross molecular beam experiments and of the theoretical studies of chemical reaction dynamics (see the reviews of the field by Casavecchia 2000; Levine 2005) have led to measurements and calculations of state-specific reaction rates for several neutral-neutral reactions (e.g. O(³P) + H₂($v = 1$) → OH($v = 1$) + H by Balakrishnan 2004). For a few reactions these studies have even provided detailed diagrams of the most probable state of the products depending on the reagent excitation state and the collision energy (Casavecchia 2000 and references therein). Similarly, the recent improvements in the flowing afterglow apparatus and the ion trapping techniques (Gerlich & Borodi 2009) have led to the first experimental deductions of state-specific rate coefficients of C⁺ + H₂ ⇌ CH⁺ + H: depending on the internal energy of H₂ (up to $v = 1$) for the forward reaction (Hierl et al. 1997) and on the internal energy of CH⁺ (up to $J = 3$) for the reverse process (Plasil et al. 2011). In particular, Plasil et al. (2011) showed that the destruction rate of CH⁺($J = 0$) by reactive collisions with H is 2 to 30 times lower than that of rotationally excited CH⁺.

To include the CH⁺ state-to-state chemistry, we followed the approach described by Black (1998) and van der Tak et al. (2007).

- We considered that CH⁺(Λ, v, J) is mainly destroyed by reactions with H, H₂, and e⁻ or by photodissociation. Because of lack of information, we also assumed that the three last reactions are independent of Λ , v , and J by adopting generic reaction rates for all levels: $k_{H_2}^D = 1.2 \times 10^{-9} \text{ cm}^3 \text{ s}^{-1}$, $k_{e^-}^D = 1.5 \times 10^{-7} (T_D/300 \text{ K})^{-0.42} \text{ cm}^3 \text{ s}^{-1}$, and $k_\gamma^D = \int \frac{4\pi}{h\nu} \sigma^\gamma(\nu) I_\nu d\nu \text{ s}^{-1}$ for reactions with H₂ and e⁻ and for the photodissociation respectively (McEwan et al. 1999; Mitchell 1990; van Dishoeck et al. 2006), where T_D is the temperature of the reaction and $\sigma^\gamma(\nu)$ are the CH⁺ photodissociation cross-

sections computed by Kirby et al. (1980). Conversely, we adopted the state-specific rates of Plasil et al. (2011) for the destruction of CH⁺ by collisions with H atoms.

- During the chemical formation of CH⁺ we assumed that the rotational level populations follow a Boltzmann distribution at the temperature of the reaction T_F :

$$k_{\Lambda, v, J}^F = k^F (2J + 1) \times \exp(-E_{\Lambda, v, J}/T_F) / \mathcal{Q}(T_F), \quad (7)$$

where k^F is the state-averaged formation rate and $\mathcal{Q}(T_F)$ is the partition function of CH⁺.

The formation and destruction temperatures correspond to the collision energies of the reagents and thus depend on their individual dynamics and on the kinetic temperature of the gas. However, since our subsequent analysis is based on the results of static models at chemical equilibrium, we assumed in the following $T_D = T_F = T_K$, unless specified otherwise. Because the dynamical properties of the gas are neglected, this hypothesis is a lower limit on the actual values of T_D and T_F .

2.5. Critical parameter analysis

In practice, all the above processes are not necessarily significant over the entire domain of parameters, namely the density of the gas n_H (in cm⁻³), the kinetic temperature T_K (in K), and the intensity of the radiation field at all wavelengths I_ν (in erg cm⁻² s⁻¹ Hz⁻¹ sr⁻¹). Moreover, if they are all included in the radiative transfer models, they can lead to computational errors when the populations of the high-energy levels are too small. It is therefore useful to make a preliminary exploration of the parameter domain and reduce, if necessary, the number of levels and excitation processes considered depending on the physical conditions of the gas. To do so, we used the analytical treatment of the main de-excitation mechanisms that we present in Appendix A. In addition to the critical density $n_{H \text{ cri}, i}$, we derived for each level i of a molecule four dimensionless critical parameters: $X_{\text{cri}, i}$, $Y_{\text{cri}, i}$, $Z_{\text{cri}, i}$, and $S_{\text{cri}, i}$ which depend on the reactive and nonreactive collisional rates, the abundances relative to H of the collision partners, the Einstein spontaneous emission

coefficients, and the intensities of the radiation field at the corresponding wavelengths.

Given the energies and the lifetimes of the $\Lambda \geq 1$ or $\nu \geq 1$ levels, collisional de-excitation of vibrational and electronic levels are found to be always negligible compared to radiative de-excitation. More importantly, our approach shows that the parameter space is divided for each rotational level into six regions where the de-excitation occurs mainly by (1) reactive collisions, (2) nonreactive collisions, (3) pure rotational, (4) rovibrational, (5) rovibronic radiative transitions, and (6) photodissociation. For example, if $n(\text{H}_2)/n_{\text{H}} = [\text{H}_2] = 0.5$ and $n(e^-)/n_{\text{H}} = [e^-] = 10^{-4}$, the limits of the first five regions for CH⁺ in the level $\Lambda, \nu, J = 0, 0, 1$ are $T_{\text{K}} \sim 800$ K, $n_{\text{H}} \sim 10^7$ cm⁻³, $I_{\nu}(4 \mu\text{m}) \sim 2 \times 10^{-8}$ erg cm⁻² s⁻¹ Hz⁻¹ sr⁻¹, and $I_{\nu}(0.4 \mu\text{m}) \sim 7 \times 10^{-12}$ erg cm⁻² s⁻¹ Hz⁻¹ sr⁻¹.

Since the excitation processes are not included, the critical parameter approach is insufficient to calculate the distribution of a molecule among its levels. However, it proves useful to point out the physical conditions for which several excitation and de-excitation mechanisms have to be taken into account and the level populations must be computed with non-LTE radiative transfer models.

3. Radiative transfer modelling

3.1. Method: the MADEX code

Table 3. Reference parameters used in Eqs. 8 - 14 to compute the interstellar radiation field at high Galactic latitude. Numbers in parenthesis are power of 10.

frequency domain	index	T (K)	τ	ν (GHz)	β
microwave	CMB	2.7			
far-infrared	fir	18	1.7 (-05)	1.1 (3)	2.0
mid-infrared 1	mi ₁	50	2.5 (-08)	2.9 (3)	1.0
mid-infrared 2	mi ₂	260	3.0 (-10)	1.5 (4)	1.5
near-infrared	nir	3000	6.0 (-13)	1.8 (5)	1.0

To study the individual impact of all pumping processes and compute the steady-state level populations of CH⁺ in several astrophysical environments, we improved and updated the MADEX (MADrid molecular spectroscopy EXcitation) excitation code (Cernicharo 2012). MADEX is a radiative transfer model based on the multi-shell high velocity gradients (LVG) formalism (Goldreich & Kwan 1974). The physical model consists of a spherical (or plan parallel) cloud of gas and dust defined by the radial (or perpendicular) profiles of the density n_{H} ; the H₂, He, and e^- abundances relative to H, [He], [H₂], and [e^-]; the CH⁺ column density $N(\text{CH}^+)$; the kinetic temperature T_{K} ; the expansion velocity of the cloud along the line of sight v_{exp} ; and the dust abundance and temperature n_d and T_d .

Gas and dust are pervaded by an internal radiation field emitted by a central star with a radius R_{\star} and an effective temperature T_{\star} , and an external radiation field defined by its specific intensity I_{ν} . To cover a broad range of the electromagnetic spectrum, the external radiation field is modelled in a simple and versatile

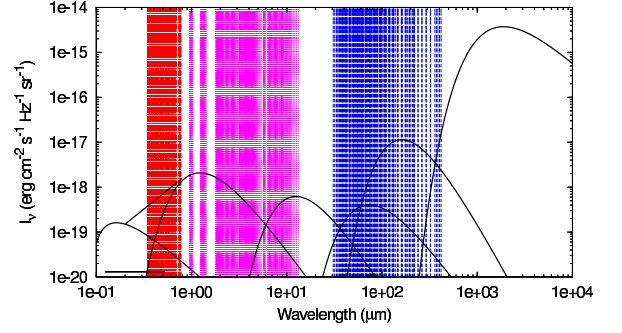


Figure 2. Interstellar radiation field intensity I_{ν} at high Galactic latitude from Table 3 and Eqs. 8 - 14 as a function of the wavelength. The wavelengths of the 1725 allowed pure rotational, rovibrational, and rovibronic radiative transitions of CH⁺ are also displayed in blue, purple, and red, taking into account the first two, five, and thirteen electronic, vibrational, and rotational levels of CH⁺.

manner as

$$I_{\nu} = \frac{2h\nu^3}{c^2} \frac{1}{\exp(h\nu/kT_{\text{CMB}}) - 1} \quad (8)$$

$$+ \frac{2h\nu^3}{c^2} \frac{\chi_{\text{fir}}}{\exp(h\nu/kT_{\text{fir}}) - 1} \left[1 - \exp(-\tau_{\text{fir}}(\nu/\nu_{\text{fir}})^{\beta_{\text{fir}}}) \right] \quad (9)$$

$$+ \frac{2h\nu^3}{c^2} \frac{\chi_{\text{mi}_1}}{\exp(h\nu/kT_{\text{mi}_1}) - 1} \left[1 - \exp(-\tau_{\text{mi}_1}(\nu/\nu_{\text{mi}_1})^{\beta_{\text{mi}_1}}) \right] \quad (10)$$

$$+ \frac{2h\nu^3}{c^2} \frac{\chi_{\text{mi}_2}}{\exp(h\nu/kT_{\text{mi}_2}) - 1} \left[1 - \exp(-\tau_{\text{mi}_2}(\nu/\nu_{\text{mi}_2})^{\beta_{\text{mi}_2}}) \right] \quad (11)$$

$$+ \frac{2h\nu^3}{c^2} \frac{\chi_{\text{nir}}}{\exp(h\nu/kT_{\text{nir}}) - 1} \left[1 - \exp(-\tau_{\text{nir}}(\nu/\nu_{\text{nir}})^{\beta_{\text{nir}}}) \right] \quad (12)$$

$$+ \chi_{\text{opt}} 9.4 \cdot 10^6 \nu^{-1.7} \text{ if } 3.7 \times 10^{14} \leq \nu \leq 1.5 \times 10^{15} \text{ GHz} \quad (13)$$

$$+ \frac{\chi_{\text{uv}}}{4\pi} \left[\frac{6.36 \cdot 10^{-17} \nu^2}{c^3} - \frac{1.02 \cdot 10^{-21} \nu^3}{c^4} + \frac{4.08 \cdot 10^{-27} \nu^4}{c^5} \right], \quad (14)$$

where Eqs. 8 - 14 correspond to the cosmic microwave background emission, the emissions of the three dust components, the large amorphous carbon and silicates, the small amorphous carbon grains, and the PAHs², as well as the emission of cold, A-type, and OB-type stars. As a reference, the temperatures and opacity laws of these functions were chosen to match the interstellar radiation field at high Galactic latitude in the ultraviolet (Draine 1978; Henry et al. 1980), optical (van Dishoeck 1988; Kopp 1996), near-infrared (Moskalenko et al. 2006), mid-infrared (Arendt et al. 1998; Compiègne et al. 2011), and far-infrared (Lagache et al. 1999; Finkbeiner et al. 1999) domains. Each component can also be adjusted using the scaling factors χ_{fir} , χ_{mi_1} , χ_{mi_2} , χ_{nir} , χ_{opt} , and χ_{uv} . The reference parameters are given in Table 3 and the corresponding specific intensity of the local interstellar radiation field is displayed in Fig. 2, along with the wavelengths of the pure rotational, rovibrational, and rovibronic transitions of CH⁺.

² for the sake of simplicity, a smooth emission function is adopted, neglecting the PAHs band emitters (Draine & Li 2007; Compiègne et al. 2011).

Lastly, the absorption of the internal and external radiation fields at near-infrared, optical, and ultraviolet wavelengths by dust particles across the cloud is taken into account in MADEX assuming the extinction curve A_λ derived by Fitzpatrick (1999) and the relation $A_V = N_H (\text{cm}^{-2})/1.8 \times 10^{21}$ (Predehl & Schmitt 1995) between the visual extinction A_V and the total column density N_H .

3.2. Analysis of the main excitation pathways

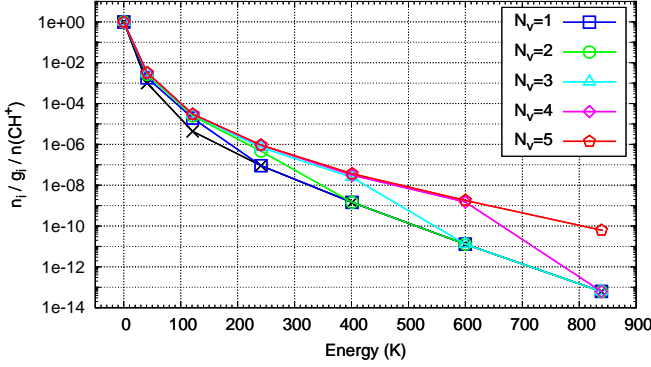


Figure 3. CH⁺ steady-state normalized excitation diagrams computed with MADEX assuming $n_H = 10^4 \text{ cm}^{-3}$, $T_K = 50 \text{ K}$, $\chi_{\text{opt}} = 10^5$, and $N(\text{CH}^+) = 10^{13} \text{ cm}^{-2}$. The number of vibrational levels taken into account within the $X^1\Sigma^+$ and $A^1\Pi$ electronic states varies between one (blue squares) and five (red pentagons). We also display for comparison the predictions of MADEX if the radiative pumping processes are switched off (black crosses).

Our first goal was to find the optical, near-infrared, and far-infrared radiation fields required to perturb the steady-state rotational level populations from what they would be in the absence of radiative pumping. Therefore, while more advanced models are discussed in the next section, we consider here a spherical cloud of gas only (no extinction from dust) without a central star and with constant density, temperature, and chemical composition. Moreover, to focus on the radiative pumping of bound rovibronic states, we intentionally neglected in a first step the photodissociation process. For $[\text{H}_2] = 0.5$, $[\text{He}] = 0.1$, $[e^-] = 10^{-4}$, $N(\text{CH}^+) = 10^{13} \text{ cm}^{-2}$, and $v_{\text{exp}} = 1 \text{ km s}^{-1}$, we computed 75600 models (for a total computing time of ~ 19 hours):

- three densities: $n_H = 10^3 \times 10^{i-1}$ for $i = 1$ to 3;
- 60 kinetic temperatures: $T_K = 30 \times 1.06^{i-1}$ for $i = 1$ to 60;
- 140 far-infrared, near-infrared, and optical radiation fields: $\chi_{\text{fir}} = 10^3 \times 1.09^{i-1}$ for $i = 1$ to 140, $\chi_{\text{nir}} = 1$, and $\chi_{\text{opt}} = 1$, $\chi_{\text{fir}} = 1$, $\chi_{\text{nir}} = 10^6 \times 1.09^{i-1}$ for $i = 1$ to 140, and $\chi_{\text{opt}} = 1$, and $\chi_{\text{fir}} = 1$, $\chi_{\text{nir}} = 1$, and $\chi_{\text{opt}} = 10^2 \times 1.11^{i-1}$ for $i = 1$ to 140,

i.e. exploring the parameter space below the limits set by the critical parameters analysis (see Sect. 2.5 and Appendix A). The dominant excitation and de-excitation mechanisms are discussed in Appendix B and are shown in Fig. B.1. As expected for this parameter range, the de-excitation of the rotational levels mainly occurs via the pure rotational radiative transitions for all models. Conversely, Fig. B.1 reveals five different excitation regimes.

1. In the limit of low kinetic temperature, the reactive collisions are responsible for the excitation of the $J \geq 1$ rotational levels, implying $n_{00J} \propto n_H \exp(-E_{00J}/T_K)$ (see Eq. B.1) at the steady-state equilibrium.
2. In the limit of high kinetic temperature, the $J \geq 1$ rotational levels are excited through chemical pumping of a high-energy rotational state (e.g. $J = 10$) followed by the radiative decay of all intermediate J states. Interestingly, the nonreactive collisions contribute to less than 20 % of the rotational excitation even for high values of T_K .
3. In the limit of large far-infrared radiation field, the rotational excitation occurs through the successive excitations of all intermediate rotational levels by direct absorption of far-infrared photons. At the steady-state equilibrium, we derive $n_{00J} \propto \chi_{\text{fir}}^J$ (see Eq. B.3).
4. In the limit of large near-infrared radiation field, the pure rotational levels are excited by near-infrared pumping of the first vibrational level of the $X^1\Sigma^+$ state. Since the transition dipole moments M_{0v00} (for $v > 1$) are at least two orders of magnitude smaller than M_{0100} (see Table 2), the pumping of the $v > 1$ levels has a negligible contribution. Moreover, because the transitions are restricted to $\Delta J = \pm 1$, the density of CH⁺ in the level J results from the successive excitations of all intermediate levels. Consequently, the high- J levels are more difficult to populate and are more sensitive to the intensity of the near-infrared radiation field: at steady-state $n_{00J} \propto \chi_{\text{nir}}^{(J+1)/2}$ and $n_{00J} \propto \chi_{\text{nir}}^{J/2}$ (see Eqs. B.4 & B.5) for odd and even values of J .
5. Finally, in the limit of large optical radiation field, the pure rotational levels are excited via the optical pumping of the first rotational levels of the $A^1\Pi$ vibronic states followed by the radiative decay through the rovibronic levels of the $X^1\Sigma^+$ state. As shown in Fig. B.1, the selection rules imply that all vibrational levels $v \leq J-2$ are required to accurately compute the population of the pure rotational level J . This result is illustrated in Fig. 3, which displays the normalized excitation diagrams of CH⁺ (up to $J = 6$) computed with MADEX for $n_H = 10^4 \text{ cm}^{-3}$, $T_K = 50 \text{ K}$, $\chi_{\text{opt}} = 10^5$ and taking into account an increasing number of vibrational levels (from 1 to 5). Lastly, since the excitations of all pure rotational levels ultimately originate from the same transition $\Lambda, v, J = 1, v, 1 \leftarrow 0, 0, 0$, their populations are equally sensitive to the intensity of the optical radiation field: $n_{00J} \propto \chi_{\text{opt}}$ (see Eq. B.6) for all $J \geq 1$ at the steady-state.

3.3. Radiation field required to activate the radiative pumping

With our grid of models we derived the radiation field intensities above which the far-infrared, near-infrared, and optical pumpings play a dominant role in populating the excited levels of CH⁺. These limits are displayed in Fig. 4 for the $J \leq 5$ rotational levels as functions of the kinetic temperature and the density. The main excitation processes are found to exponentially depend on T_K , as was already predicted in the previous section. In addition, the superimposition of the curves computed at different densities confirms their dependence on n_H and J derived analytically in Appendix B.

Fig. 4 shows that the interaction with the far-infrared radiation competes with the collisional processes in the rotational excitation of CH⁺ for $\chi_{\text{fir}} \geq 10^4 \times (n_H/10^4)^{1/J}$. Similarly, the pumping of the vibrational states could influence the populations of the low- J rotational levels, providing that the gas is pervaded by a near-infrared radiation field at least $10^7 \times (n_H/10^4)^{2/J}$

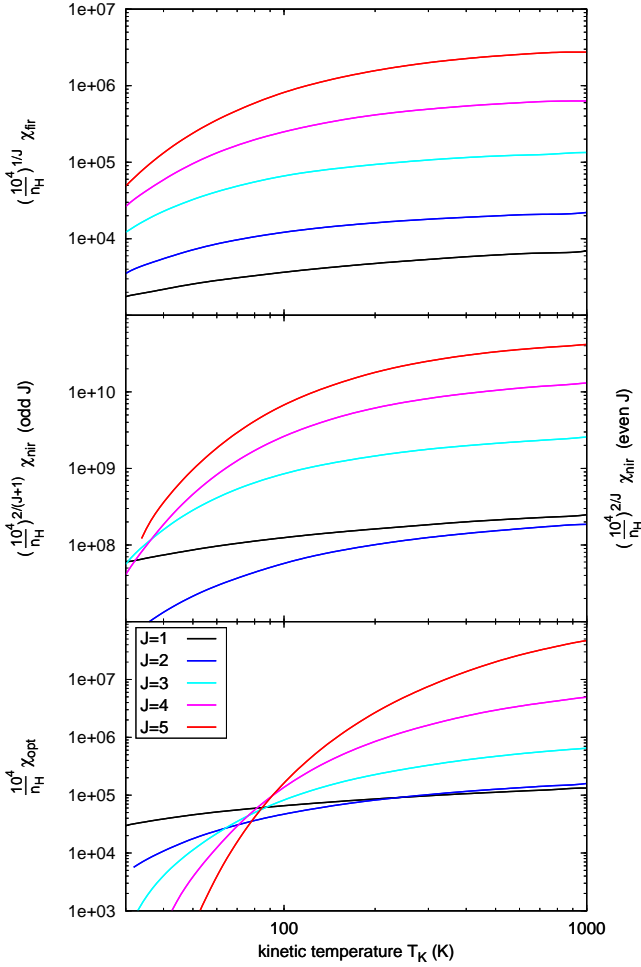


Figure 4. Far-infrared (top), near-infrared (middle), and optical (bottom) radiation fields (in units of the local ISRF) at which the pure rotational levels of CH⁺ are equally populated by collisions and radiative pumping, depending on the kinetic temperature and the density of the gas. Below these curves, excitations are primarily driven by reactive collisions and chemical pumping. Above these curves, excitations are primarily driven by direct radiative pumping (top) and by the radiative pumping of the vibrational levels of the X¹Σ⁺ state (middle) and of the A¹Π electronic state (bottom).

and $10^8 \times (n_{\text{H}}/10^4)^{2/J}$ times larger than the local ISRF for $T_{\text{K}} < 100$ K and $T_{\text{K}} > 100$ K. Lastly, an optical radiation field of $\sim 10^5 \times (n_{\text{H}}/10^4)$ the local ISRF is required to activate the pumping of bound electronic states for $T_{\text{K}} > 100$ K, while this limit drops at lower kinetic temperatures.

3.4. Impact of the photodissociation

As emphasized in Appendix A, the impact of the photodissociation on the rotational excitation of CH⁺ strongly depends on the spectrum of the UV radiation field. For instance, while the photodissociation is negligible compared to bound-bound electronic transitions in a radiation field emitted by a black body with an effective temperature $< 10^4$ K, the two processes have comparable rates in the standard interstellar radiation field. Therefore the photodissociation could play an important role in the rota-

tional excitation of CH⁺ in any environment in which the A¹Π - X¹Σ⁺ pumping competes with the collisional processes (Fig. 4 bottom).

Hereafter, we therefore included the photodissociation process into MADEX and applied a model to several astronomical sources with different values of T_{K} , $\chi_{\text{fir}}/n_{\text{H}}$, $\chi_{\text{nir}}/n_{\text{H}}$, and $\chi_{\text{opt}}/n_{\text{H}}$. The following questions were addressed: how do the predictions of MADEX compare with the available observations? How do all these excitation processes modify our understanding of the physical conditions of the interstellar and circumstellar matter?

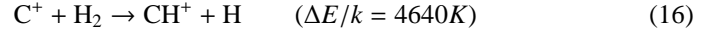
4. Application to astronomical sources

4.1. Chemical formation of CH⁺

Because an efficient production pathway is required to balance its rapid destruction by hydrogenation and dissociative recombination, CH⁺ is believed to be formed either via



in environments submitted to a strong X-ray radiation field (e.g. the central molecular zone, Langer 1978), or by the highly endothermic reaction



in other Galactic environments. So far, two main scenarios have been invoked to overcome the endothermicity of reaction 16: (1) by the release of supra-thermal energy, induced for example by magnetohydrodynamic shocks, in regions with large reservoirs of kinetic and magnetic energies (e.g. Draine 1986; Xie et al. 1995; Falgarone et al. 1995); and (2) by the internal energy of H₂ (Hierl et al. 1997; Agúndez et al. 2010) in regions where the vibrational levels of H₂ are excited by FUV fluorescence.

For each astronomical source considered below, we therefore applied an appropriate chemical model to describe the abundance distributions of CH⁺ and of its main collisional partners. To investigate the origine of the rotational excitation of CH⁺ we then systematically ran MADEX in three different configurations: ❶ considering only the excitation by nonreactive collisions, ❷ considering all collisional excitation processes (i.e. including the chemical pumping), and ❸ considering all excitation processes (i.e. including the radiative pumping and the photodissociation). The parameters and results of all models are summarized in Table 4, where we compare the continuum-subtracted line fluxes (or continuum-subtracted line intensities) of CH⁺ computed with MADEX with the available observations.

4.2. Diffuse interstellar medium

We first focus on the cold diffuse interstellar matter characterized by a low density and by low $\chi_{\text{nir}}/n_{\text{H}}$ and $\chi_{\text{opt}}/n_{\text{H}}$ ratios. The observed mean column density of CH⁺, $\log_{10}(N(\text{CH}^+)/N_{\text{H}}) \sim -8.11 \pm 0.33$ (from a compilation of data: Crane et al. 1995; Gredel 1997; Weselak et al. 2008; Falgarone et al. 2010; Godard et al. 2012) has been proposed to trace low-velocity magnetohydrodynamic shocks (Pineau des Forêts et al. 1986), Alfvén waves (Federman et al. 1996), turbulent mixing (Lesaffre et al. 2007), or turbulent dissipation (Joulain et al. 1998). According to the TDR (turbulent dissipation region) model of Godard et al. (2009), CH⁺ is formed in regions where turbulent dissipation is triggered by the decoupling of the ionized and neutral flows at small spatial scales (~ 100 AU). In these regions, the kinetic temperature increases to ~ 1000 K,

Table 4. Comparison between the observed intensities $\int Idv$ or fluxes $\iint Idvd\Omega$ of the rotational lines of CH⁺ and those predicted by MADEX for the selected astronomical sources. In all cases, MADEX was run in the three configurations ①, ②, and ③ (see main text), and the far-infrared continuum emission was removed in the computation of the line intensities.

parameter	cold diffuse medium				Orion Bar				NGC 7027			
n_{H} (cm ⁻³)	50				5×10^4				2×10^5			
χ_{opt}	1 - 50				3×10^4				4×10^4			
χ_{nir}	1 - 50				3×10^4				2×10^5			
χ_{fir}	1 - 10				1				1			
T_{fir}	18				55				150			
τ_{fir}	1.7×10^{-5}				5×10^{-2}				1×10^{-2}			
β_{fir}	2.0				1.75				0.5			
v_{exp} (km s ⁻¹)	5				10				20			
Ω (sr)					2.7×10^{-8}				1.2×10^{-9}			
transition	intensity (in 10^{-10} erg s ⁻¹ cm ⁻² sr ⁻¹)				flux (in 10^{-14} erg s ⁻¹ cm ⁻²)				flux (in 10^{-19} W cm ⁻²)			
	①	②	③	obs ^a	①	②	③	obs ^b	①	②	③	obs ^c
$J = 1 - 0$	2.7	4.5	5.9	< 79	9.3	11.8	11.8	11.1 ± 1.8	0.4	0.5	0.5	0.47 ± 0.01
$J = 2 - 1$	3.7	7.1	9.5	< 480	13.2	18.1	18.3		1.6	2.0	2.0	1.51 ± 0.05
$J = 3 - 2$	2.4	7.0	9.7		6.7	13.8	13.9		2.1	2.5	2.5	2.18 ± 0.17
$J = 4 - 3$	2.3	7.7	1.1		6.1	13.4	13.5		1.6	2.1	2.1	2.00 ± 0.22
$J = 5 - 4$	1.1	6.6	9.6		3.0	8.3	8.4		1.1	1.7	1.7	2.50 ± 0.41
$J = 6 - 5$	1.1	6.3	9.2		2.9	7.5	7.6		0.7	1.3	1.3	2.41 ± 0.33

^a detection limits computed with the rms noise level of the CH⁺ (1 - 0) and (2 - 1) spectra with the Herschel/HIFI instrument (Godard et al. 2012; M. Gerin, priv. comm.); ^b from Naylor et al. (2010) and Habart et al. (2010); ^c from Cernicharo et al. (1997) and Wesson et al. (2010).

while the CH⁺ formation temperature is boosted by the ion-neutral velocity drift up to ~ 2000 K. Assuming a density $n_{\text{H}} = 50$ cm⁻³ and a moderate shielding $A_{\text{V}} > 0.2$ of the interstellar radiation field ($\chi_{\text{opt}} = \chi_{\text{nir}} = \chi_{\text{fir}} = 1$), most of the hydrogen is in molecular form and the ionization degree is $\sim 10^{-4}$.

These properties were injected into MADEX to compute the beam-averaged continuum-subtracted intensities of the CH⁺ rotational lines (see Table 4) assuming that the turbulent dissipation regions have a surface filling factor of 1. We find that the pumping by near- and far-infrared radiation has no influence on the excitation of the rotational levels of CH⁺ even if $\chi_{\text{nir}} = 50$ and $\chi_{\text{fir}} = 10$, i.e. adopting the highest energy density of the interstellar radiation field derived by Moskalenko et al. (2006) across the Galactic disk. In contrast, the optical pumping and the photodissociation are found to be non-negligible compared to the collisional processes for $\chi_{\text{uv/opt}} \geq 10$, i.e. in the most central regions ($R_{\text{g}} < 4$ Kpc, Moskalenko et al. 2006) of the Milky Way. For instance, for $\chi_{\text{uv/opt}} = 50$, the optical pumping and the photodissociation contribute up to 30 % of the rotational excitation of CH⁺ (Col. 4 of Table 4). In all cases, we finally find that the intensities of the two first rotational emission lines predicted by MADEX are at least 14 times smaller than the limit of detection of the Herschel/HIFI data (Godard et al. 2012), in agreement with the fact that CH⁺ has only been detected in the diffuse interstellar medium in absorption towards strong submillimeter continuum sources.

4.3. Hot and dense PDRs: e.g. the Orion Bar

We selected the Orion Bar as a prototypical hot and dense PDR with an high $\chi_{\text{opt}}/n_{\text{H}}$ ratio. Lying at a distance of 414 ± 7 pc (Menten et al. 2007), the Bar consists of a homogeneous interclump medium with a density $n_{\text{H}} \sim 5 \times 10^4$ cm⁻³ (Young Owl et al. 2000), located approximately $111''$ (~ 0.22 pc) south-east of the Trapezium star cluster (Pellegrini et al. 2009). The resulting incident UV and optical radiation fields

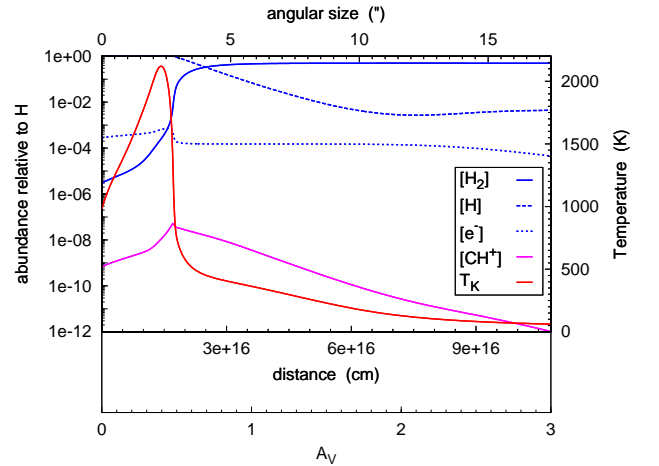


Figure 5. Kinetic temperature and abundances relative to H of H₂, H, e⁻, and CH⁺ computed with the Meudon PDR code as functions of the extinction (bottom axis), the distance (middle axis), and the angular size (top axis) across the Orion Bar starting from the ionization front.

at the ionization front are $\sim 3 \times 10^4$ that of the local ISRF (Marconi et al. 1998). The near-infrared continuum emission of the HII region corresponds to 10^4 that of the local ISRF (Walmsley et al. 2000). Lastly, the recent observations at 70, 160, 250, 350, and 500 μm performed by Arab et al. (2012) using the PACS and SPIRE instruments of the Herschel space telescope have revealed dust temperature and spectral index gradients from 80 K to 40 K and from 1.2 to 2.2 from the ionization front to the Orion molecular cloud, respectively.

With all these parameters, we computed the chemical profile of the Orion Bar with the Meudon PDR code, a one-dimensional chemical model in which a static slab of gas of given thickness

is illuminated on one side or on both sides by a given FUV radiation field (Le Petit et al. 2006). Fig. 5 displays the physical structure of the Orion Bar predicted by the most recent online version of the Meudon PDR code³, which takes into account the influence of vibrationally excited H₂ in the formation of CH⁺ (Agúndez et al. 2010). Inserting the density profiles of H, H₂, e⁻, and CH⁺ into MADEX and taking into account the geometry of the bar described by Hogerheijde et al. (1995), we finally derived the six first rotational line fluxes of CH⁺ (integrated over a 36'' wide solid angle, after having removed the far-infrared continuum emission) given in columns 6, 7, and 8 of Table 4.

The comparison of models ①, ②, and ③ shows that the radiative pumping and the photodissociation have only a marginal effect ($\leq 2\%$) on the excitation of the rotational levels of CH⁺. In contrast, even if the high-*J* transitions appear to be mostly driven by chemical pumping, both reactive and nonreactive collisions are required to accurately model all the far-infrared emission lines of CH⁺. At last, the flux of the CH⁺ *J* = 1–0 transition derived with MADEX is found to agree well with the value observed by Naylor et al. (2010) and Habart et al. (2010) using the Herschel/SPIRE instrument. This result indicates that the emission lines of CH⁺ detected in the Orion Bar probably arise from the interclump medium rather than from dense and hot regions ($T_K \sim 200$ K and $n_H \sim 10^7$ cm⁻³, Goicoechea et al. 2011). Since the *J* = 3–2 transition of CH⁺ detected with Herschel/PACS was found to spatially correlate with the 60–100 μm rotational lines of OH (Goicoechea et al. 2011) and the high-*J* rotational lines of CO detected with Herschel/SPIRE (Habart et al. 2010), this result also suggests that chemical formation and/or radiative pumping could have a significant impact on the rotational excitation of OH and CO in the Orion Bar PDR. If this is the case, clumps would no longer be required to account for their observed emission line intensities (Goicoechea et al. 2011).

4.4. Planetary nebulae: e.g. NGC 7027

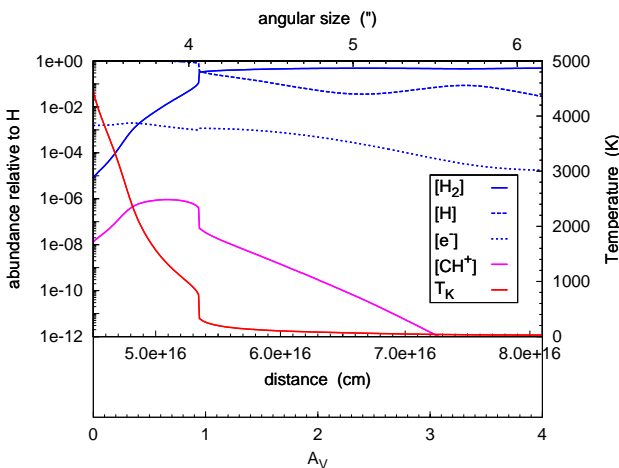


Figure 6. Kinetic temperature and abundances relative to H of H₂, H, e⁻, and CH⁺ computed with the Meudon PDR code as functions of the extinction (bottom axis) across the PDR region of NGC 7027 starting from the ionization front. The distance and the angle from the central star are indicated along the middle and top axes.

Lastly, we chose NGC 7027 as an archetypal planetary nebula with an high χ_{nir}/n_H ratio. Located at a distance of 880 ± 150 pc (Masson 1989), NGC 7027 is composed of ionized, atomic, and molecular C-rich shells surrounding a single central star with an effective temperature $T_\star \sim 198,000$ K and a radius $R_\star \sim 5.21 \times 10^9$ cm (Latter et al. 2000). The ionized shell revealed by a strong near-infrared continuum emission has an ellipsoidal morphology with dimensions $6'' \times 12''$, while the borders of the PDR traced by the emission lines of H₂ have a biconical structure with dimensions $10'' \times 13''$ (Latter et al. 2000; Cox et al. 2002). The molecular envelope detected in CO and other millimetric molecular transitions extends up to $\sim 100''$ in radius (Navarro et al. 2003).

For the sake of simplicity, we modelled the PDR region as a spherical shell with dimensions set to match the molecular emission lines observed along the minor axis of NGC 7027 (Cox et al. 2002). The ionization front is located at $3.4''$ (~ 0.0145 pc) from the central star, implying an incident UV radiation field of $\sim 3 \times 10^4$ that of the local ISRF (Hasegawa et al. 2000). Using the optical and near-infrared spectra modelled by Volk & Kwok (1997) and the extinction curve found by Zhang et al. (2003), we estimate that the incident optical and near-infrared radiation fields are $\sim 4 \times 10^4$ and $\sim 2 \times 10^5$ times stronger than the local ISRF at $0.4 \mu\text{m}$ and $4 \mu\text{m}$. Finally, the far- and mid-infrared dust emission are modelled as a single grey body with a temperature $T_{\text{fir}} = 150$ K, an opacity $\tau_{\text{fir}} = 10^{-5}$, and a spectral index $\beta_{\text{fir}} = 0.5$ to reproduce the continuum emission observed by Dyck & Simon (1976) and Terzian (1989). In contrast to the work of previous authors (Cox et al. 2002; Hasegawa et al. 2000; Yan et al. 1999), who proposed PDR models including a high-density shell, we considered only the low-density PDR component defined by $n_H = 2 \times 10^5$ cm⁻³.

In the same way as for the Orion Bar PDR, the chemical composition of NGC 7027 was computed with the Meudon PDR code, i.e. assuming that the radial structure of the source is well described with a plan-parallel model. The carbon-rich circumstellar envelope was modelled with C, O, N, and S elemental abundances of 1.3×10^{-3} , 5.5×10^{-4} , 1.9×10^{-4} , and 7.9×10^{-6} (Middlemass 1990). The resulting chemical and temperature profiles are shown in Fig. 6 as functions of the distance from the central star. The fluxes of the rotational emission lines of CH⁺ (integrated over a $9''$ wide solid angle, after removing the far-infrared continuum emission, see Table 4) were finally calculated, assuming that the chemical composition has a spherical symmetry and taking into account the influence of the limb brightening.

Because of the high kinetic temperature and electronic fraction, the nonreactive collisions of CH⁺ with e⁻ pilot the distribution of CH⁺ among the low-*J* rotational levels, and even compete with the chemical pumping in the excitation of the high-*J* transitions. Our main result is that the predictions of MADEX agree excellently with the observations performed by Cernicharo et al. (1997) using the ISO/SWS instrument and with those of Wesson et al. (2010) using the Herschel/SPIRE instrument. Furthermore, because all collisional excitation processes are included in MADEX, the intensities of all observed rotational lines are explained with a circumstellar medium of density $n_H = 2 \times 10^5$, a value 10 to 100 times lower than those inferred from traditional excitation models (Cernicharo et al. 1997; Hasegawa et al. 2000; Yan et al. 1999).

³ version 1.4.4 available at <http://pdr.obspm.fr/PDRcode.html>

4.5. Summary

We conclude from these applications that the far-infrared pumping, the near-infrared and optical fluorescences, and the photodissociation have a marginal impact on the far-infrared emission lines of CH⁺. For all the sources considered, the excitations of the high- J and low- J lines mainly arise from chemical pumping and from a combination of chemical pumping and nonreactive collisional processes. For low- J lines, the balance of these two mechanisms then principally depends on the chemical composition of the gas and the kinetic temperature. For instance, in environments with a large electronic fraction, such as the C-rich PDRs (e.g. NGC 7027), the nonreactive collisions with electrons are found to dominate the rotational excitation of CH⁺ up to the $J = 4 - 3$ transition.

Our main result is that the comparison between the observed line fluxes and the predictions of MADEX points towards interstellar and circumstellar media with densities far lower than those deduced with traditional models. This study thus proves the importance of exploring all possible excitation pathways of a molecule before drawing any conclusion on the physical structure and geometry of the source. In particular, we question the degree of clumpiness of the Orion Bar molecular cloud.

We therefore recommend to treat any other astronomical environments detected in CH⁺ in a similar way. For instance, the rotational lines of CH⁺ have recently been observed by Thi et al. (2011) in the protoplanetary disc that surrounds the Herbig Be star HD 100546 using the Herschel/PACS instrument. Considering only the excitation by nonreactive collisions, Thi et al. (2011) found that the strong emission lines of CH⁺ (up to $J = 6 - 5$) arise from the rim of the outer disc and the disc surface, i.e. from media predominantly atomic with densities $\sim 10^8$ cm⁻³ and temperatures $\sim 10^2 - 10^3$ K. With an effective temperature of the central star ~ 10500 K (van den Ancker et al. 1997), the photodissociation is unlikely to have any effect on the distribution of CH⁺ among its rotational levels (see Appendix A). Conversely, the strong flux of optical photons could enhance the high- J level populations at the disc surface where the CH⁺ abundance is the highest. Moreover, with the chemical composition described by Thi et al. (2011), we expect the chemical pumping to dominate the nonreactive collisional processes. It would thus be interesting to estimate how the chemical and radiative pumping affect the understanding of the density structure of the disc and of the spatial emission of rotationally excited CH⁺.

In preparation of future investigations, we present below an extension of our model to other diatomic molecules with spectroscopic characteristics similar to those of CH⁺.

5. Discussion: extension to other diatomic molecules

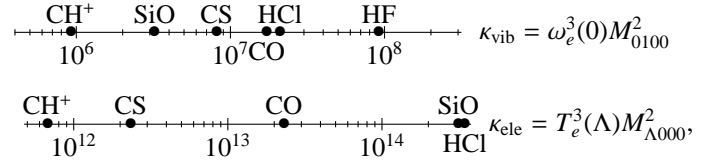
5.1. Analytical considerations of the excitation timescales

The analysis of the main excitation pathways performed in Appendix B shows that the pumping processes of CH⁺ can be easily described by a set of analytical formulae. This result is inherent to the $X^1\Sigma^+$ ground-state electronic configuration of CH⁺ since the associated transition rules favour only one specific excitation pipeline among all others (see Fig. B.1). Consequently, the radiative pumping almost solely depends on the rotational, vibrational, and vibronic Einstein spontaneous emission coefficients, which are proportional to $\nu^3 M_{0000}^2$, $\nu^3 M_{0\nu'0\nu''}^2$, and $\nu^3 M_{1\nu'0\nu''}^2$ for the far-infrared, near-infrared, and optical/UV

pumpings. In this section, we focus only on the near-infrared and optical/UV pumpings.

While polyatomic molecules and other ground-state electronic configurations will be treated in forthcoming papers (e.g. NH₃, OH(²Π), and CO⁺(²Σ⁺) in priority), we thus select here several $X^1\Sigma^+$ ground-state diatomic molecular species characterized by different vibrational and vibronic Einstein coefficients: two light hydrides HF and HCl, and three heavy molecules SiO, CS, and CO. Since we aim at providing complete excitation models of these chemical compounds, we took into account their main bound electronic configurations: the $A^1\Pi$ states of CO, CS, and SiO, the $E^1\Sigma^+$ state of SiO characterized by high transition probabilities (Elander & Smith 1973), and the $C^1\Pi$ state of HCl. Conversely, we ignore the $A^1\Pi$ states of HF and HCl, which are known to correspond to repulsive configurations (Bender & Davidson 1968; Lee 1999), and the $B^1\Sigma^+ - X^1\Sigma^+$ system of HF, whose Franck-Condon factors are found negligible for the $\nu' \leq 10$, $\nu'' = 0$ bands (Alvaríño et al. 1983). Lastly, because the rotational, vibrational, and electronic structures of these species are clearly separated in energy, and because we aim to draw conclusions from their fundamental spectroscopic properties, we reduced their effective Hamiltonian to the three prime molecular constants $T_e(\Lambda)$, $\omega_e(\Lambda)$, and $B_e(\Lambda)$.

Within this approximation, the molecules considered are organized as follows:



where κ_{vib} and κ_{ele} are inversely proportional to the lifetimes of the excited vibrational and electronic states. According to these schemes and without any other considerations, CH⁺ appears to be the species the least sensitive to both the near-infrared and optical/UV pumpings. In contrast, the vibrational transition dipole moment of HF and the electronic transition dipole moments of SiO and HCl are so high that HF, and SiO and HCl are likely candidates to radiative pumpings by near-infrared and optical/UV photons. In the following, we compare this simple analytical study with the results obtained with MADEX, and we identify the fundamental excitation mechanisms of HF, HCl, SiO, CS, and CO, depending on the spectrum of the radiation field pervading a PDR-type medium of constant density $n_{\text{H}} = 10^4$ cm⁻³ and temperature $T_{\text{K}} = 100$ K.

The spectroscopic properties and the nonreactive collisional rates of HF, HCl, SiO, CS, and CO were implemented in our modified version of the MADEX code, along with their respective chemical destruction rates and photodissociation rates, both inferred at the border of the PDR from the Meudon PDR code. Except for CH⁺, we only considered H, H₂, and He as collisional partners in the computation of the nonreactive nonelastic collisional rates, thus neglecting the excitation via electron impact (see, e.g., Thummel et al. 1992; Itikawa & Mason 2005). In the same way as for CH⁺, MADEX was then run, assuming PDR-type conditions and solar metallicities, in four different configurations: ❶ considering only the excitation by nonreactive collisions, ❷ considering all collisional excitation processes (i.e. including the chemical pumping), ❸ considering all line excitation processes (i.e. including the radiative pumping of bound vibronic levels), and ❹ considering all radiative processes (i.e. including the photodissociation) with different values of the near-infrared and optical/UV scaling factors χ_{NIR} and

$\chi_{\text{opt/UV}}$. The molecular constants, the transition dipole moments, the collisional rates, and the results of all models are given in Tables 5, 6, and 7. For comparison, we also display in Table 5 the results of this analysis applied to CH⁺.

5.2. Species sensitive to chemical pumping

With the chemical destruction rates considered as typical in PDR-type environments (see Tables 5-7), we find that CH⁺ is the only species, among those considered, with low- J levels sensitive to its chemical formation. This concurs with the idea that chemical pumping essentially applies to short-lived molecules, and in particular to molecular ions with lifetimes below $10^{-2}(10^4/n_{\text{H}})$ yr (e.g. CO⁺, Stäuber & Bruderer 2009). Indeed, the chemical pumping has a marginal impact on HCl, SiO, CS, and CO because the timescales of the nonreactive collisional excitation of the $J \leq 5$ levels are at least one order of magnitude lower than their respective destruction timescales.

We note, however, that this last statement should not be generalized to the high- J levels. As was already stressed in Sect. 4.5, the importance of chemical pumping relative to nonreactive collisions increases with J . For instance, Table 6 shows that the chemical formation takes over the excitation of the rotational levels of HF for $J \geq 3$. This suggests that this mechanism could play a dominant role for all species, especially in environments with a kinetic temperature close to the equivalent temperatures of the rovibrational transitions. A direct application could be the interpretation of the high- J CO lines observed during the past decade in protoplanetary and planetary nebulae, protostellar shocks, and dense and hot PDRs with the KAO, SOFIA, ISO, and all the instruments onboard the Herschel space observatory (Justtanont et al. 1997; Bujarrabal et al. 2010; Benedettini et al. 2012; Habart et al. 2010). If the chemical formation efficiently pumps the high- J lines of CO, the high densities $n_{\text{H}} > 10^6$ of the CRL 618 and NGC 7027 molecular clouds inferred from CO emission up to the $J = 22 - 21$ transition by Justtanont et al. (1997) and Bujarrabal et al. (2010) would be revised to lower values. The chemical pumping could similarly offer an alternative understanding of low-mass protostellar outflows where the high- J lines of CO (up to $J = 38 - 37$) observed by van Kempen et al. (2010) with Herschel/PACS have been proposed to trace the UV irradiation of the outflow cavity walls and small-scale C-type shocks propagating along the cavity walls (Visser et al. 2012).

5.3. Species sensitive to radiative pumping by near-infrared photons

The comparison of models ② and ③ shows that HF and HCl are the two species the most sensitive to the intensity of the near-infrared radiation field. In contrast, the near-infrared fluorescence is found to have almost no influence on the populations of the rotational levels of CH⁺ and SiO and only a marginal effect on those of CS and CO. When cross-compared, these behaviours originate from a combination of factors: (1) the nonreactive collisional rates of HCl and HF (except for the $1 - 0$ transition) are ~ 3 to 10 times lower than those of CH⁺, SiO, CS, and CO; and (2) the lifetimes of the vibrational levels of HF, HCl, CO, CS, SiO, and CH⁺ increase from HF to CH⁺ over two orders of magnitude. It follows that the organization of the species based on their sensitivity to radiative pumping of their vibrational states agrees well with the classification we inferred from the sole analysis of the κ_{vib} values (see Sect. 5.1).

Quantitatively, the populations of the $J = 1, 2, 3$ levels of HF increase by a few percent to more than a factor of 10 for χ_{nir} varying between 10^3 and 10^5 . A similar result is found for the $J = 1, 2, 3$ levels of HCl, although it requires near-infrared intensities ~ 10 times higher. Finally, minimum near-infrared radiation fields of $\sim 10^6$ and $\sim 10^7$ times that of the local ISRF are needed to efficiently activate the radiative pumping of CS and CO on one side and of SiO on the other side.

Overall, the main tracer of near-infrared fluorescence is the $J = 2 - 1$ transition of HF. Unfortunately, this line has, so far, only been observed in absorption towards Sagittarius B2, (Neufeld et al. 1997). In turn, the fact that the $J = 1$ level of HF is slightly enhanced from $\chi_{\text{nir}} = 10^3$ to 10^5 is in accordance with the model of van der Tak et al. (2012), who argued that the electron impact excitation is sufficient to explain the HF ($1 - 0$) emission line observed in the Orion Bar interclump medium with Herschel/HIFI.

5.4. Species sensitive to radiative pumping of bound electronic states by optical and UV photons

The predictions of MADEX concerning the excitation by optical and UV pumping of bound electronic states are also found to agree well with the analysis of the κ_{ele} values carried out in Sect. 5.1. As predicted, SiO and HCl, and to a lesser extent CO, are sensitive to the optical and UV radiation field intensities in the configuration ④, while CH⁺ and CS are not. More precisely, we find that the populations of the $J \geq 3$ and $J \geq 4$ levels of SiO and CO increase by more than a factor of 2 via the pumping of their A¹Π electronic states for an optical/UV radiation field larger than 10^3 and 10^4 (in Draine's unit) respectively. For $\chi_{\text{opt/UV}} = 10^4$, we find that this process even induces a population inversion of the $J = 0$ and $J = 1$ rotational levels of SiO. This remarkable behaviour contrasts with that of CH⁺ and CS, whose rotational level populations are influenced by optical and UV pumping only for a radiation field 10^5 times larger than the local ISRF.

The applications of the radiative pumping of bound electronic states of SiO extend to a variety of astronomical sources. Observed in the Orion Bar and S 140 PDRs by Schilke et al. (2001), the high- J (up to $J = 5 - 4$) and low- J ($J = 2 - 1$ and $J = 3 - 2$) rotational lines of SiO have been thought to trace clumps with densities of $2 \times 10^6 \text{ cm}^{-3}$ and molecular clouds at lower densities (down to a few 10^4 cm^{-3}), respectively. With the predictions of Table 5, we estimate, on the contrary, that the entire SiO emission originates from the low-density component and that the high- J lines are confined to the border of the PDR where the radiative pumping is maximal. In addition to reproducing the SiO rotational diagram, this last result is in concordance with the extended nature of the SiO ($2 - 1$) emission – compared to that of SiO ($5 - 4$) – observed in the Orion Bar PDR.

Similar conclusions may be drawn for the high-velocity molecular outflows of class 0 protostars, where the high- J (up to $11 - 10$) rotational lines of SiO associated to the molecular bullets distant from the central star are detected with intensities considerably lower than those measured in the bullets close to the driving source (Nisini et al. 2002, 2007). Originally attributed to density gradients (Nisini et al. 2007), this behaviour may be explained with the dilution of the strong FUV radiation field emitted by the young stellar object along the outflow cavity (e.g. Bruderer et al. 2009).

Finally, the radiative pumping by optical and UV photons could play a major role on the production of the SiO masers

observed in the region between the photosphere and the dust-growth zone of evolved stars envelopes (e.g. Gray et al. 1995; Cernicharo et al. 1993 and references therein). With the transition dipole moments of SiO given in Table 5, this process is expected to drive the excitation of the $\nu \geq 2$ levels, in contradiction to Bujarrabal (1994), who proposed direct infrared pumping of the $\Delta\nu = 1$ transitions as a global inversion process. In a subsequent paper, we will confront the predictions of our complete excitation model to the forthcoming survey of SiO maser emission (up to $\nu = 6$) performed on a sample of 50 O-rich evolved stars (in preparation).

5.5. Species sensitive to their photodissociation

Finally, Tables 5, 6, and 7 show that the photodissociation processes have a substantial effect on the rotational diagrams of all species considered for $\chi_{\text{opt/UV}}$ varying between 10^2 and 10^4 . In particular, the photodissociation, whose rates are derived for an optical/UV flux scaling with the standard ISRF, is found to compete with the bound-bound absorption of optical/UV photons by SiO, CO, and CH⁺, and even to dominate the bound-bound absorption of optical/UV photons by HCl and CS.

The species the most sensitive to this mechanism are HF, HCl, and to a lesser extent CS. For instance, we find that the photodissociation drives the populations of the $J \geq 4$ levels of HF and HCl and of the $J \geq 3$ levels of CS, providing that the gas is illuminated by a UV radiation field 10^2 and 10^3 times that of the local ISRF. Moreover, since the photodissociation acts as an additional chemical destruction rate, its impact on the level populations is similar to the chemical pumping and thus increases with J .

These results suggest that the photodissociation may influence the rotational diagrams of all the species singled out in Sect. 5.2, 5.3, and 5.4. We note, however, that the importance of the process relative to the chemical pumping and the radiative pumping of bound states strongly depends on the chemical composition of the gas and the spectrum of the optical/UV field. We therefore recommend to use models that compute the coupling between the radiative transfer and the chemical evolution of the gas to accurately describe the excitation of molecules detected in bright PDRs.

6. Conclusions and perspectives

We have performed a theoretical investigation of the main excitation and de-excitation mechanisms of the methylidyne cation in several astrophysical environments. To do so, we built a new version of the MADEX radiative transfer model that not only includes all rotational, rovibrational, and rovibronic transitions of CH⁺, but also takes into account the excitation induced by reactive and nonreactive collisions. The model was used to estimate the optical and near-infrared radiation fields required to perturb the steady-state rotational level populations of CH⁺, and also to provide valuable predictions of the intensities of its far-infrared emission lines. The results of MADEX were systematically compared with an extensive analytical study of the pumping processes of CH⁺, which we finally used to extend our predictions to five other $X^1\Sigma^+$ ground-state diatomic molecules, HF, HCl, SiO, CS, and CO.

A remarkable agreement was found, throughout this paper, between the results of MADEX and the analytical description, thus giving access to the dependence of the excitation processes on the main physical conditions of the gas (n_{H} , T_{K} , and I_{ν}) and on

the fundamental spectroscopic properties of the molecule considered. The key parameters that govern the strength of the radiative pumping of the vibrational and bound $^1\Pi$ electronic states of a given species are $\kappa_{\text{vib}} = \omega_e^3(0)M_{0100}^2$ and $\kappa_{\text{ele}} = T_e^3(1)M_{1000}^2$. It follows that the far-infrared and submillimetric lines of HF and HCl (SiO, HCl and CO) strongly depend on the intensity of the near-infrared (optical/UV) radiation field in astrophysical environments submitted to a photon flux at least $10^3 \times (n_{\text{H}}/10^4)$ and $10^4 \times (n_{\text{H}}/10^4)$ times the value observed in the solar neighbourhood. Such environments include bright PDRs where the photodissociation is expected to compete with the line processes in the rotational excitation of the molecules. The species the most sensitive to the photodissociation are HF and HCl, whose rotational diagrams are affected by a UV flux as low as $10^2 \times (n_{\text{H}}/10^4)$ times that of the local ISRF. In contrast, the distribution of populations among the rotational levels of CH⁺ is weakly sensitive to both the radiative pumping of bound states and the photodissociation, and is found to strongly depend on the CH⁺ chemical formation.

As a natural consequence, the intensities of the pure rotational lines of CH⁺ observed towards the Orion Bar and the NGC 7027 PDRs are reproduced with MADEX assuming molecular clouds with proton densities of 5×10^4 and $2 \times 10^5 \text{ cm}^{-3}$, respectively. Our estimate of the density of the NGC 7027 circumstellar PDR is one to two orders of magnitude below the value inferred from traditional excitation models. In addition, we found that the CH⁺ emission originates from the interclump medium of the Orion Bar PDR, which contradicts the spatial correlation found between the CH⁺ (3–2) emission line and the high-density tracers such as the rotational Λ -doublets of OH and high- J rotational transitions of CO. Consequently, all our results favour molecular clouds with densities significantly lower than previously established.

It is foreseeable that similar investigations will have to be carried out for all molecules detected in interstellar and circumstellar molecular clouds. In forthcoming papers we will address in priority the following problems.

1. The radiative pumping of the $A^1\Pi$ and $E^1\Sigma^+$ electronic levels of SiO may have a dominant role in the production of SiO masers in the envelopes of evolved stars. We intend to perform a statistical analysis of the inversion process based on the comparison of the predictions of MADEX with the forthcoming observations of the SiO masers in the high vibrational states (up to $\nu = 6$) in a sample of 50 O-rich evolved stars covering a wide range of mass loss rates.
2. Because the efficiency of the radiative pumping highly depends on the electronic configuration of the considered species, we plan to extend the predictions of MADEX to $^3\Sigma^+$ and $^2\Pi$ ground-state diatomic molecules. Our goal is to study two molecules that are believed to trace media with high density and temperature, CO⁺ and OH.

Acknowledgements. We are most grateful to Franck Le Petit, Edith Falgarone, and John Black for providing judicious comments on this manuscript and helping to improve its content. We also thank the Spanish MICINN for funding support through grants AYA2009-07304 and CSD2009-00038.

References

- Agúndez, M., Cernicharo, J., Waters, L. B. F. M., et al. 2011, *A&A*, 533, L6
 Agúndez, M., Fonfría, J. P., Cernicharo, J., Pardo, J. R., & Guélin, M. 2008, *A&A*, 479, 493
 Agúndez, M., Goicoechea, J. R., Cernicharo, J., Faure, A., & Roueff, E. 2010, *ApJ*, 713, 662

- Alvariño, J. M., González, L. F., Hernández, M. L., & Martínez, E. 1983, *Spectroscopy Letters*, 16, 541
- Arab, H., Abergel, A., Habart, E., et al. 2012, *A&A*, 541, A19
- Arendt, R. G., Odegard, N., Weiland, J. L., et al. 1998, *ApJ*, 508, 74
- Balakrishnan, N. 2004, *J. Chem. Phys.*, 121, 6346
- Balm, S. P. & Jura, M. 1992, *A&A*, 261, L25
- Barrow, R. F. & Stone, T. J. 1975, *Journal of Physics B Atomic Molecular Physics*, 8, L13
- Beer, R., Lambert, D. L., & Sneden, C. 1974, *PASP*, 86, 806
- Bender, C. F. & Davidson, E. R. 1968, *The Journal of Chemical Physics*, 49, 4989
- Benedettini, M., Busquet, G., Lefloch, B., et al. 2012, *A&A*, 539, L3
- Black, J. H. 1998, *Faraday Discussions*, 109, 257
- Black, J. H. & van Dishoeck, E. F. 1987, *ApJ*, 322, 412
- Botschwina, P. & Sebald, P. 1985, *Journal of Molecular Spectroscopy*, 110, 1
- Brown, J. M., Colbourn, E. A., Watson, J. K. G., & Wayne, F. D. 1979, *Journal of Molecular Spectroscopy*, 74, 294
- Brown, J. M., Hougen, J. T., Huber, K.-P., et al. 1975, *Journal of Molecular Spectroscopy*, 55, 500
- Bruderer, S., Benz, A. O., Stäuber, P., & Doty, S. D. 2010, *ApJ*, 720, 1432
- Bruderer, S., Doty, S. D., & Benz, A. O. 2009, *ApJS*, 183, 179
- Bujarrabal, V. 1994, *A&A*, 285, 953
- Bujarrabal, V., Alcolea, J., Soria-Ruiz, R., et al. 2010, *A&A*, 521, L3
- Carre, M. 1968, *Physica*, 41, 63
- Carrington, A. & Ramsay, D. A. 1982, *Phys. Scr*, 25, 272
- Carroll, T. J. & Goldsmith, P. F. 1981, *ApJ*, 245, 891
- Casavecchia, P. 2000, *Reports on Progress in Physics*, 63, 355
- Cernicharo, J. 2012, in *Proceedings of the European Conference on Laboratory Astrophysics*, European Astronomical Society Publications Series, ed. C. Stehlé, C. Joblin, & L. d'Hendecourt
- Cernicharo, J., Bujarrabal, V., & Santaren, J. L. 1993, *ApJ*, 407, L33
- Cernicharo, J., Liu, X.-W., Gonzalez-Alfonso, E., et al. 1997, *ApJ*, 483, L65
- Chackerian, C. & Tipping, R. H. 1982, *Journal of Molecular Spectroscopy*, 93, 237
- Chantranupong, L. 1992, *Chemical Physics*, 161, 351
- Cheng, M., Brown, J. M., Rosmus, P., et al. 2007, *Phys. Rev. A*, 75, 012502
- Compiègne, M., Verstraete, L., Jones, A., et al. 2011, *A&A*, 525, A103
- Cox, P., Huggins, P. J., Maillard, J.-P., et al. 2002, *A&A*, 384, 603
- Crane, P., Lambert, D. L., & Sheffer, Y. 1995, *ApJS*, 99, 107
- Dayou, F. & Balança, C. 2006, *A&A*, 459, 297
- Douglas, A. E. & Herzberg, G. 1941, *ApJ*, 94, 381
- Draine, B. T. 1978, *ApJS*, 36, 595
- Draine, B. T. 1986, *ApJ*, 310, 408
- Draine, B. T. & Li, A. 2007, *ApJ*, 657, 810
- Drira, I., Hure, J. M., Spielfiedel, A., Feautrier, N., & Roueff, E. 1997, *A&A*, 319, 720
- Drira, I., Spielfiedel, A., Edwards, S., & Feautrier, N. 1998, *J. Quant. Spec. Radiat. Transf.*, 60, 1
- Dyck, H. M. & Simon, T. 1976, *PASP*, 88, 738
- Eidelsberg, M., Benayoun, J. J., Viala, Y., et al. 1992, *A&A*, 265, 839
- Elander, N., Oddershede, J., & Beebe, N. H. F. 1977, *ApJ*, 216, 165
- Elander, N. & Smith, W. H. 1973, *ApJ*, 184, 311
- Falgarone, E., Godard, B., Cernicharo, J., et al. 2010, *A&A*, 521, L15+
- Falgarone, E., Pineau des Forêts, G., & Roueff, E. 1995, *A&A*, 300, 870
- Federman, S. R., Rawlings, J. M. C., Taylor, S. D., & Williams, D. A. 1996, *MNRAS*, 279, L41
- Finkbeiner, D. P., Davis, M., & Schlegel, D. J. 1999, *ApJ*, 524, 867
- Fitzpatrick, E. L. 1999, *PASP*, 111, 63
- Flower, D. R. 2001, *Journal of Physics B Atomic Molecular Physics*, 34, 2731
- Follmeg, B., Rosmus, P., & Werner, H.-J. 1987, *Chemical Physics Letters*, 136, 562
- Gerlich, D. & Borodi, G. 2009, *Faraday Discussions*, 142, 57
- Gerlich, D., Disch, R., & Scherbarth, S. 1987, *J. Chem. Phys.*, 87, 350
- Giard, M., Puget, J. L., Crete, E., & Scoupe, F. 1997, *A&A*, 322, 624
- Godard, B., Falgarone, E., Gerin, M., et al. 2012, *A&A*, 540, A87
- Godard, B., Falgarone, E., & Pineau Des Forêts, G. 2009, *A&A*, 495, 847
- Goicoechea, J. R., Joblin, C., Contursi, A., et al. 2011, *A&A*, 530, L16
- Goldreich, P. & Kwan, J. 1974, *ApJ*, 189, 441
- González-Alfonso, E. & Cernicharo, J. 1999, in *ESA Special Publication*, Vol. 427, *The Universe as Seen by ISO*, ed. P. Cox & M. Kessler, 325
- González-Alfonso, E., Neufeld, D. A., & Melnick, G. J. 2007, *ApJ*, 669, 412
- Goorvitch, D. 1994, *ApJS*, 95, 535
- Gray, M. D., Ivison, R. J., Yates, J. A., et al. 1995, *MNRAS*, 277, L67
- Gredel, R. 1997, *A&A*, 320, 929
- Guillon, G. & Stoecklin, T. 2012, *MNRAS*, 420, 579
- Habart, E., Dartois, E., Abergel, A., et al. 2010, *A&A*, 518, L116
- Habart, E., Walmsley, M., Verstraete, L., et al. 2005, *Space Sci. Rev.*, 119, 71
- Hakalla, R., Kępa, R., Szajna, W., & Zachwieja, M. 2006, *European Physical Journal D*, 38, 481
- Hammami, K., Owono Owono, L. C., & Jaidane, N. e. a. 2008, *Journal of Molecular structure: THEOCHEM*, 853, 18
- Hammami, K., Owono Owono, L. C., & Stäuber, P. 2009, *A&A*, 507, 1083
- Hasegawa, T., Volk, K., & Kwok, S. 2000, *ApJ*, 532, 994
- Hedelund, J. & Lambert, D. L. 1972, *Astrophys. Lett.*, 11, 71
- Henry, R. C., Anderson, R. C., & Fastie, W. G. 1980, *ApJ*, 239, 859
- Herzberg, G. 1950, *Molecular spectra and molecular structure. Vol.1: Spectra of diatomic molecules*, ed. Herzberg, G.
- Hierl, P. M., Morris, R. A., & Viggiano, A. A. 1997, *J. Chem. Phys.*, 106, 10145
- Hogerheijde, M. R., Jansen, D. J., & van Dishoeck, E. F. 1995, *A&A*, 294, 792
- Itikawa, Y. & Mason, N. 2005, *Phys. Rep.*, 414, 1
- Johns, J. W. C. & Barrow, R. F. 1959, in *Proc. R. Soc. London A*, Vol. 251, 504
- Joulain, K., Falgarone, E., Pineau des Forêts, G., & Flower, D. 1998, *A&A*, 340, 241
- Justtanont, K., Tielens, A. G. G. M., Skinner, C. J., & Haas, M. R. 1997, *ApJ*, 476, 319
- Kirby, K., Roberge, W. G., Saxon, R. P., & Liu, B. 1980, *ApJ*, 239, 855
- Kiriyama, F. & Rao, B. S. 2001, *Journal of Quantitative Spectroscopy & Radiative Transfer*, 65, 673
- Kopp, M. 1996, PhD thesis, Université Paris XI, (1996)
- Krotkov, R., Wang, D., & Scoville, N. Z. 1980, *ApJ*, 240, 940
- Lagache, G., Abergel, A., Boulanger, F., Désert, F. X., & Puget, J.-L. 1999, *A&A*, 344, 322
- Langer, W. D. 1978, *ApJ*, 225, 860
- Larsson, M. 1983, *A&A*, 128, 291
- Latter, W. B., Dayal, A., Bieging, J. H., et al. 2000, *ApJ*, 539, 783
- Le Petit, F., Nehmé, C., Le Bourlot, J., & Roueff, E. 2006, *ApJS*, 164, 506
- Lee, S. 1999, *Bull. Korean Chem. Soc.*, 20, 987
- Lesaffre, P., Gerin, M., & Hennebelle, P. 2007, *A&A*, 469, 949
- Levine, R. D. 2005, *Molecular Reaction Dynamics*
- Li, G., Gordon, I. E., Bernath, P. F., & Rothman, L. S. 2011, *J. Quant. Spec. Radiat. Transf.*, 112, 1543
- Lim, A. J., Rabadán, I., & Tennyson, J. 1999, *MNRAS*, 306, 473
- Lique, F. & Spielfiedel, A. 2007, *A&A*, 462, 1179
- Liszt, H. S. & Smith, W. H. 1972, *J. Quant. Spec. Radiat. Transf.*, 12, 1591
- Lovas, F. J. & Kruppenie, P. H. 1974, *Journal of Physical and Chemical Reference Data*, 3, 245
- Macris, C. & Petropoulos, B. 1985, *Ap&SS*, 116, 165
- Marconi, A., Testi, L., Natta, A., & Walmsley, C. M. 1998, *A&A*, 330, 696
- Masson, C. R. 1989, *ApJ*, 336, 294
- McEwan, M. J., Scott, G. B. I., Adams, N. G., et al. 1999, *ApJ*, 513, 287
- Menten, K. M., Reid, M. J., Forbrich, J., & Brunthaler, A. 2007, *A&A*, 474, 515
- Meredith, R. 1973, *J. Quant. Spec. Radiat. Transf.*, 13, 89
- Middlemass, D. 1990, *MNRAS*, 244, 294
- Mitchell, J. B. A. 1990, *Phys. Rep.*, 186, 215
- Morris, M. 1975, *ApJ*, 197, 603
- Moskalenko, I. V., Porter, T. A., & Strong, A. W. 2006, *ApJ*, 640, L155
- Müller, H. S. P. 2010, *A&A*, 514, L6
- Naidu, G. 1981, *Physica B+C*, 106, 308
- Navarro, S. G., Corradi, R. L. M., & Mampaso, A. 2003, in *Revista Mexicana de Astronomía y Astrofísica*, vol. 27, Vol. 18, *Revista Mexicana de Astronomía y Astrofísica Conference Series*, ed. M. Reyes-Ruiz & E. Vázquez-Semadeni, 75–77
- Naylor, D. A., Dartois, E., Habart, E., et al. 2010, *A&A*, 518, L117
- Neufeld, D. A. & Green, S. 1994, *ApJ*, 432, 158
- Neufeld, D. A., Zmuidzinas, J., Schilke, P., & Phillips, T. G. 1997, *ApJ*, 488, L141
- Nisini, B., Codella, C., Giannini, T., & Richer, J. S. 2002, *A&A*, 395, L25
- Nisini, B., Codella, C., Giannini, T., et al. 2007, *A&A*, 462, 163
- Park, C. S., Crosley, D. R., Eckstrom, D. J., & Heere, K. R. 1993, *J. Quant. Spec. Radiat. Transf.*, 49, 349
- Pearson, J. C. & Drouin, B. J. 2006, *ApJ*, 647, L83
- Pellegrini, E. W., Baldwin, J. A., Ferland, G. J., Shaw, G., & Heathcote, S. 2009, *ApJ*, 693, 285
- Pineau des Forêts, G., Roueff, E., & Flower, D. R. 1986, *MNRAS*, 223, 743
- Plasil, R., Mehner, T., Dohnal, P., et al. 2011, *ApJ*, 737, 60
- Predehl, P. & Schmitt, J. H. M. M. 1995, *A&A*, 293, 889
- Rank, D. H., Rao, B. S., & Wiggins, T. A. 1965, *Journal of Molecular Spectroscopy*, 17, 122
- Reese, C., Stoecklin, T., Voronin, A., & Rayez, J. C. 2005, *A&A*, 430, 1139
- Roueff, E., Felenbok, P., Black, J. H., & Gry, C. 2002, *A&A*, 384, 629
- Schilke, P., Pineau des Forêts, G., Walmsley, C. M., & Martín-Pintado, J. 2001, *A&A*, 372, 291
- Scoville, N. Z., Krotkov, R., & Wang, D. 1980, *ApJ*, 240, 929
- Stäuber, P. & Bruderer, S. 2009, *A&A*, 505, 195
- Stoecklin, T. & Voronin, A. 2008, *Eur. Phys. J. D*, 46, 259
- Sundholm, D., Olsen, J., & Jørgensen, P. 1995, *J. Chem. Phys.*, 102, 4143

- Terzian, Y. 1989, in IAU Symposium, Vol. 131, Planetary Nebulae, ed. S. Torres-
Peimbert, 17–28
- Thi, W.-F., Ménard, F., Meeus, G., et al. 2011, A&A, 530, L2
- Thummel, H. T., Nesbet, R. K., & Peyerimhoff, S. D. 1992, Journal of Physics
B Atomic Molecular Physics, 25, 4553
- Tilford, S. G., Ginter, M. L., & Vanderslice, J. T. 1970, Journal of Molecular
Spectroscopy, 33, 505
- Tipping, R. H. & Chackerian, Jr., C. 1981, Journal of Molecular Spectroscopy,
88, 352
- Troutman, M. R., Hinkle, K. H., Najita, J. R., Rettig, T. W., & Brittain, S. D.
2011, ApJ, 738, 12
- Turner, B. E., Chan, K.-W., Green, S., & Lubowich, D. A. 1992, ApJ, 399, 114
- Turpin, F., Stoecklin, T., & Voronin, A. 2010, A&A, 511, A28
- van den Ancker, M. E., The, P. S., Tjin A Djie, H. R. E., et al. 1997, A&A, 324,
L33
- van der Tak, F. F. S., Black, J. H., Schöier, F. L., Jansen, D. J., & van Dishoeck,
E. F. 2007, A&A, 468, 627
- van der Tak, F. F. S., Ossenkopf, V., Nagy, Z., et al. 2012, A&A, 537, L10
- van Dishoeck, E. F. 1988, in Rate Coefficients in Astrochemistry. Proceedings of
a Conference held in UMIST, Manchester, United Kingdom, September 21–
24, 1987. Editors, T.J. Millar, D.A. Williams; Publisher, Kluwer Academic
Publishers, Dordrecht, Boston, 1988. ISBN # 90-277-2752-X. LC # QB450
.R38 1988. P. 49, 1988, ed. T. J. Millar & D. A. Williams, 49
- van Dishoeck, E. F. & Black, J. H. 1982, ApJ, 258, 533
- van Dishoeck, E. F., Jonkheid, B., & van Hemert, M. C. 2006, Faraday
Discussions, 133, 231
- van Dishoeck, E. F., van Hemert, M. C., & Dalgarno, A. 1982, J. Chem. Phys.,
77, 3693
- van Kempen, T. A., Kristensen, L. E., Herczeg, G. J., et al. 2010, A&A, 518,
L121
- Visser, R., Kristensen, L. E., Bruderer, S., et al. 2012, A&A, 537, A55
- Volk, K. & Kwok, S. 1997, ApJ, 477, 722
- Walmsley, C. M., Natta, A., Oliva, E., & Testi, L. 2000, A&A, 364, 301
- Webb, D. U. & Narahari Rao, K. 1968, Journal of Molecular Spectroscopy, 28,
121
- Weselak, T., Galazutdinov, G. A., Musaev, F. A., Beletsky, Y., & Kretowski, J.
2009, A&A, 495, 189
- Weselak, T., Galazutdinov, G. A., Musaev, F. A., & Kretowski, J. 2008, A&A,
484, 381
- Wesson, R., Cernicharo, J., Barlow, M. J., et al. 2010, A&A, 518, L144
- Winnewisser, G. & Cook, R. L. 1968, Journal of Molecular Spectroscopy, 28,
266
- Xie, T., Allen, M., & Langer, W. D. 1995, ApJ, 440, 674
- Yan, M., Federman, S. R., Dalgarno, A., & Bjorkman, J. E. 1999, ApJ, 515, 640
- Young Owl, R. C., Meixner, M. M., Wolfire, M., Tielens, A. G. G. M., & Tauber,
J. 2000, ApJ, 540, 886
- Zhang, Y., Liu, X.-W., & Luo, S.-G. 2003, in IAU Symposium, Vol. 209,
Planetary Nebulae: Their Evolution and Role in the Universe, ed. S. Kwok,
M. Dopita, & R. Sutherland, 319

Appendix A: Analysis of the dominant de-excitation processes of CH⁺

The concept of critical density – density at which the nonreactive collisional de-excitation rate equals the radiative decay rate – provides valuable insight into the mechanism that controls the population of each level of a molecule depending on the physical conditions of the gas. However, this concept is insufficient if state-to-state chemistry is taken into account, or if the wavelengths of the radiative de-excitations of the level considered span a wide range of the electromagnetic spectrum, as is the case if rovibrational or rovibronic transitions are considered. We therefore address the following question: in this general case, can we derive a set of critical parameters that will give us insight into what the steady-state level populations should be depending on the conditions of the gas?

We consider a species S whose levels are characterized by three quantum numbers only, the total orbital angular momentum Λ , the vibrational momentum ν , and the total angular momentum J . Taking into account all radiative and collisional processes, the density of atoms n_i in the level i (with a degeneracy

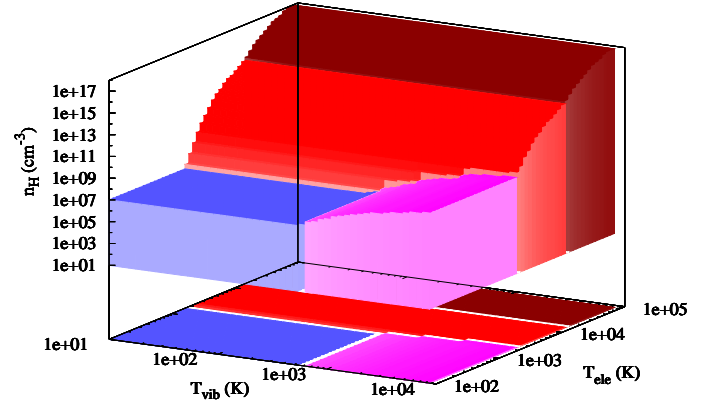


Figure A.1. Dominant de-excitation process of CH⁺ $J = 1$ as a function of the density n_H , and the equivalent black body temperatures T_{vib} and T_{ele} , for $T_{\text{rot}} = 2.7$ K. In the blue, purple, red, and brown regions, the de-excitation of CH⁺ $J = 1$ is dominated by pure rotational, rovibrational, and rovibronic radiative transitions and by the photodissociation. In the empty space above, the de-excitation occurs through reactive and nonreactive collisions depending on T_K and the chemical composition of the gas (see main text).

g_i) verifies, at steady-state,

$$n_i = \frac{\sum_F n_{F_a} n_{F_b} k_i^F + \sum_c \sum_j n_c n_j k_{ij}^c + \sum_j n_j (A_{ji} + \langle n_{\gamma,\nu} \rangle A_{ji} + \frac{g_i}{g_j} \langle n_{\gamma,\nu} \rangle A_{ij})}{\sum_D n_D k_i^D + \sum_c \sum_j n_c k_{ij}^c + \sum_j (A_{ij} + \langle n_{\gamma,\nu} \rangle A_{ij} + \frac{g_j}{g_i} \langle n_{\gamma,\nu} \rangle A_{ji}) + \int \frac{4\pi}{h\nu} \sigma_i^\gamma(\nu) I_\nu d\nu} \quad (\text{A.1})$$

and

$$n(S) = \sum_i n_i \quad (\text{A.2})$$

In these formulae, n_D , n_{F_a} , and n_{F_b} are the densities of reagents that chemically destroy and form the level i at rates k_i^D and k_i^F , n_C and k_{ij}^C are the abundances of the nonreactive collision partners and the corresponding collisional rates, A_{ij} and $\langle n_{\gamma,\nu} \rangle$ are the Einstein spontaneous de-excitation coefficients and the directionally averaged photon occupation number⁴ of the radiation field at the frequency ν of the $i - j$ transition, and σ_i^γ are the photodissociation cross-sections of the level i .

To estimate the importance of the different de-excitation processes, we deliberately decomposed the radiative term of Eq. A.1 into three parts that include all transitions: (1) between two levels in the same electronic and vibrational state ($\Lambda_i = \Lambda_j$ and $\nu_i = \nu_j$), (2) between two levels in the same electronic state and different vibrational states ($\Lambda_i = \Lambda_j$ and $\nu_i \neq \nu_j$), and (3) between two levels in different electronic states ($\Lambda_i \neq \Lambda_j$). We then regrouped all processes involving high-energy photons, i.e. the bound-bound rovibronic transitions and the photodissociation. In addition, we assumed that the radiation field intensities at the corresponding frequencies are described by three black bodies with equivalent temperatures T_{rot} , T_{vib} , and T_{ele} respec-

⁴ $\langle n_{\gamma,\nu} \rangle$ is related to the radiative energy density u_ν (in erg cm⁻³ Hz⁻¹) and the radiative specific intensity I_ν (in erg cm⁻² Hz⁻¹ sterad⁻¹ s⁻¹) through : $\langle n_{\gamma,\nu} \rangle = I_\nu c^2 / 2h\nu^3$ and $u_\nu = 4\pi I_\nu / c$

tively. Re-arranging Eq. A.1, we obtain

$$\begin{aligned}
 n_i = & \left(\frac{1}{1 + \frac{n_{\text{H}}}{n_{\text{H}}^{\text{cri},i}}} \right) \left(\frac{1}{1 + \frac{X_{\text{cri},i}}{1}} \right) \frac{\sum_F n_{F,i} n_{F,b} k_i^F}{\sum_D n_D k_i^D} + \\
 & \left(\frac{1}{1 + \frac{n_{\text{H}}}{n_{\text{H}}^{\text{cri},i}}} \right) \left(\frac{1}{1 + \frac{1}{X_{\text{cri},i}}} \right) \frac{\sum_C \sum_j n_C n_j k_{ji}^C}{\sum_C \sum_j n_C k_{ji}^C} + \\
 & \left(\frac{1}{1 + \frac{n_{\text{H}}}{n_{\text{H}}^{\text{cri},i}}} \right) \left(\frac{1}{1 + \frac{Y_{\text{cri},i}}{1}} \right) \frac{\sum_{j/\Lambda_j \neq \Lambda_i} n_j (A_{ji} + \langle n_{\gamma,v} \rangle A_{ji} + \frac{g_j}{g_i} \langle n_{\gamma,v} \rangle A_{ji})}{\sum_{j/\Lambda_j \neq \Lambda_i} (A_{ij} + \langle n_{\gamma,v} \rangle A_{ij} + \frac{g_j}{g_i} \langle n_{\gamma,v} \rangle A_{ji})} + \\
 & \left(\frac{1}{1 + \frac{n_{\text{H}}}{n_{\text{H}}^{\text{cri},i}}} \right) \left(\frac{1}{1 + \frac{1}{Y_{\text{cri},i}}} \right) \left(\frac{1}{1 + \frac{Z_{\text{cri},i}}{1}} \right) \frac{\sum_{j/\Lambda_j \neq \Lambda_i} n_j (A_{ji} + \langle n_{\gamma,v} \rangle A_{ji} + \frac{g_j}{g_i} \langle n_{\gamma,v} \rangle A_{ji})}{\sum_{j/\Lambda_j \neq \Lambda_i} (A_{ij} + \langle n_{\gamma,v} \rangle A_{ij} + \frac{g_j}{g_i} \langle n_{\gamma,v} \rangle A_{ji})} + \\
 & \left(\frac{1}{1 + \frac{n_{\text{H}}}{n_{\text{H}}^{\text{cri},i}}} \right) \left(\frac{1}{1 + \frac{1}{Y_{\text{cri},i}}} \right) \left(\frac{1}{1 + \frac{1}{Z_{\text{cri},i}}} \right) \left(\frac{1}{1 + \frac{1}{S_{\text{cri},i}}} \right) \times \\
 & \frac{\sum_{j/\Lambda_j \neq \Lambda_i} n_j (A_{ji} + \langle n_{\gamma,v} \rangle A_{ji} + \frac{g_j}{g_i} \langle n_{\gamma,v} \rangle A_{ji})}{\sum_{j/\Lambda_j \neq \Lambda_i} (A_{ij} + \langle n_{\gamma,v} \rangle A_{ij} + \frac{g_j}{g_i} \langle n_{\gamma,v} \rangle A_{ji})},
 \end{aligned} \tag{A.3}$$

where each term tends to drag the level populations towards different Boltzmann distributions at temperatures T_F , T_K , T_{rot} , T_{vib} , and T_{ele} . In the previous equation we define five independent parameters, the critical total hydrogen density $n_{\text{H}}^{\text{cri},i}$ (in cm^{-3}), and four dimensionless critical ratios, $X_{\text{cri},i}$ which depend on the abundances relative to H of the reactive and nonreactive collisional partners $[D]$ and $[C]$, and $Y_{\text{cri},i}$, $Z_{\text{cri},i}$, and $S_{\text{cri},i}$, which depend on the entire spectrum of the radiation field:

$$n_{\text{H}}^{\text{cri},i} = \frac{\sum_j (A_{ij} + \langle n_{\gamma,v} \rangle A_{ij} + \frac{g_j}{g_i} \langle n_{\gamma,v} \rangle A_{ji}) + \int \frac{4\pi}{h\nu} \sigma_i^\gamma(\nu) I_\nu d\nu}{\sum_D [D] k_i^D + \sum_C [C] k_{ij}^C} \tag{A.4}$$

$$X_{\text{cri},i} = \frac{\sum_C \sum_j [C] k_{ij}^C}{\sum_D [D] k_i^D} \tag{A.5}$$

$$\begin{aligned}
 Y_{\text{cri},i} = & \frac{\sum_{j/\Lambda_j \neq \Lambda_i} (A_{ij} + \langle n_{\gamma,v} \rangle A_{ij} + \frac{g_j}{g_i} \langle n_{\gamma,v} \rangle A_{ji}) + \int \frac{4\pi}{h\nu} \sigma_i^\gamma(\nu) I_\nu d\nu}{\sum_{j/\Lambda_j \neq \Lambda_i} (A_{ij} + \langle n_{\gamma,v} \rangle A_{ij} + \frac{g_j}{g_i} \langle n_{\gamma,v} \rangle A_{ji})} \\
 & \frac{\sum_{j/\Lambda_j \neq \Lambda_i} (A_{ij} + \langle n_{\gamma,v} \rangle A_{ij} + \frac{g_j}{g_i} \langle n_{\gamma,v} \rangle A_{ji})}{\sum_{j/\Lambda_j \neq \Lambda_i} (A_{ij} + \langle n_{\gamma,v} \rangle A_{ij} + \frac{g_j}{g_i} \langle n_{\gamma,v} \rangle A_{ji})}
 \end{aligned} \tag{A.6}$$

$$Z_{\text{cri},i} = \frac{\sum_{j/\Lambda_j \neq \Lambda_i} (A_{ij} + \langle n_{\gamma,v} \rangle A_{ij} + \frac{g_j}{g_i} \langle n_{\gamma,v} \rangle A_{ji}) + \int \frac{4\pi}{h\nu} \sigma_i^\gamma(\nu) I_\nu d\nu}{\sum_{j/\Lambda_j \neq \Lambda_i} (A_{ij} + \langle n_{\gamma,v} \rangle A_{ij} + \frac{g_j}{g_i} \langle n_{\gamma,v} \rangle A_{ji})}$$

$$S_{\text{cri},i} = \frac{\sum_{j/\Lambda_j \neq \Lambda_i} (A_{ij} + \langle n_{\gamma,v} \rangle A_{ij} + \frac{g_j}{g_i} \langle n_{\gamma,v} \rangle A_{ji})}{\int \frac{4\pi}{h\nu} \sigma_i^\gamma(\nu) I_\nu d\nu}. \tag{A.8}$$

These quantities prove useful to explore the parameter domain since they indicate the main de-excitation mechanism of each level depending on the condition of the gas: through reactive collisions for $n_{\text{H}} > n_{\text{H}}^{\text{cri},i}$ and $X_{\text{cri},i} < 1$, nonreactive collisions for $n_{\text{H}} > n_{\text{H}}^{\text{cri},i}$ and $X_{\text{cri},i} > 1$, rotational radiative transitions for $n_{\text{H}} < n_{\text{H}}^{\text{cri},i}$ and $Y_{\text{cri},i} < 1$, vibrational radiative transitions for $n_{\text{H}} < n_{\text{H}}^{\text{cri},i}$, $Y_{\text{cri},i} > 1$ and $Z_{\text{cri},i} < 1$, electronic radiative transitions for $n_{\text{H}} < n_{\text{H}}^{\text{cri},i}$, $Y_{\text{cri},i} > 1$, $Z_{\text{cri},i} > 1$, and $S_{\text{cri},i} > 1$, and photodissociation for $n_{\text{H}} < n_{\text{H}}^{\text{cri},i}$, $Y_{\text{cri},i} > 1$, $Z_{\text{cri},i} > 1$, and $S_{\text{cri},i} < 1$.

When applied with the spectroscopic, collisional and chemical properties of CH⁺, the critical parameter analysis gives the following results:

- given their short lifetimes, the de-excitation of the vibrational and electronic levels of CH⁺ always occurs through spontaneous radiative emission of near-/mid-infrared and optical photons.
- The critical ratios $X_{\text{cri},J} \leq 1$ for all rotational levels $J \geq 1$ as long as $T_K \leq 710 \times (2.5 - 3.0[\text{H}_2])^{-1.9}$ K and $T_K \leq 1100 \times ([e^-]/10^{-4})^{-1}$ K. The other critical parameters mainly depend on the density of the gas and the intensity of the radiation field.

As an example, we therefore display in Fig. A.1 the limits set by the critical parameters analysis for CH⁺ in the level $\Lambda, v, J = 0, 0, 1$, assuming $[\text{H}_2] = 0.5$, $[\text{He}] = 0.1$, $[e^-] = 10^{-4}$, $T_K = 100$ K, $T_F = T_D = T_K$, and $T_{\text{rot}} = 2.7$ K. The edges at $n_{\text{H}} \sim 10^7 \text{ cm}^{-3}$, $T_{\text{vib}} \sim 630$ K, $T_{\text{ele}} \sim 1740$ K, and $T_{\text{ele}} \sim 14400$ K point to the physical conditions for which several de-excitation mechanisms have to be taken into account to accurately compute the level populations.

According to Fig. A.1, a large UV and optical radiation field seems to be required for the photodissociation to compete with the bound-bound rovibronic absorption. However, we emphasize that this result strongly depends on the functional form used to describe the radiation field, i.e. a black body with an effective temperature T_{ele} in the present case. In the standard unshielded interstellar radiation field, the photodissociation and the bound-bound rovibronic absorption are found to have comparable rates and are therefore expected to play similar roles in distributing CH⁺ among its rotational levels.

Appendix B: Analysis of the dominant excitation processes of CH⁺

Fig. B.1 shows the excitation and de-excitation pathways that drive the populations of the first five rotational levels of CH⁺ computed with MADEX and neglecting the photodissociation. Five extreme models were selected: (a) $T_K = 100$ K, $\chi_{\text{fir}} = 1$, $\chi_{\text{nir}} = 1$, and $\chi_{\text{opt}} = 1$, (b) $T_K = 1000$ K, $\chi_{\text{fir}} = 1$, $\chi_{\text{nir}} = 1$, and $\chi_{\text{opt}} = 1$, (c) $T_K = 100$ K, $\chi_{\text{fir}} = 10^6$, $\chi_{\text{nir}} = 1$, and $\chi_{\text{opt}} = 1$, (d) $T_K = 100$ K, $\chi_{\text{fir}} = 1$, $\chi_{\text{nir}} = 10^{10}$, and $\chi_{\text{opt}} = 1$, (e) $T_K = 100$ K, $\chi_{\text{fir}} = 1$, $\chi_{\text{nir}} = 1$, and $\chi_{\text{opt}} = 10^6$, assuming $N(\text{CH}^+) = 10^{13} \text{ cm}^{-2}$, $v_{\text{exp}} = 1 \text{ km s}^{-1}$, and $n_{\text{H}} = 10^4 \text{ cm}^{-3}$. This figure is simplified: for each level, only the processes that together contribute to

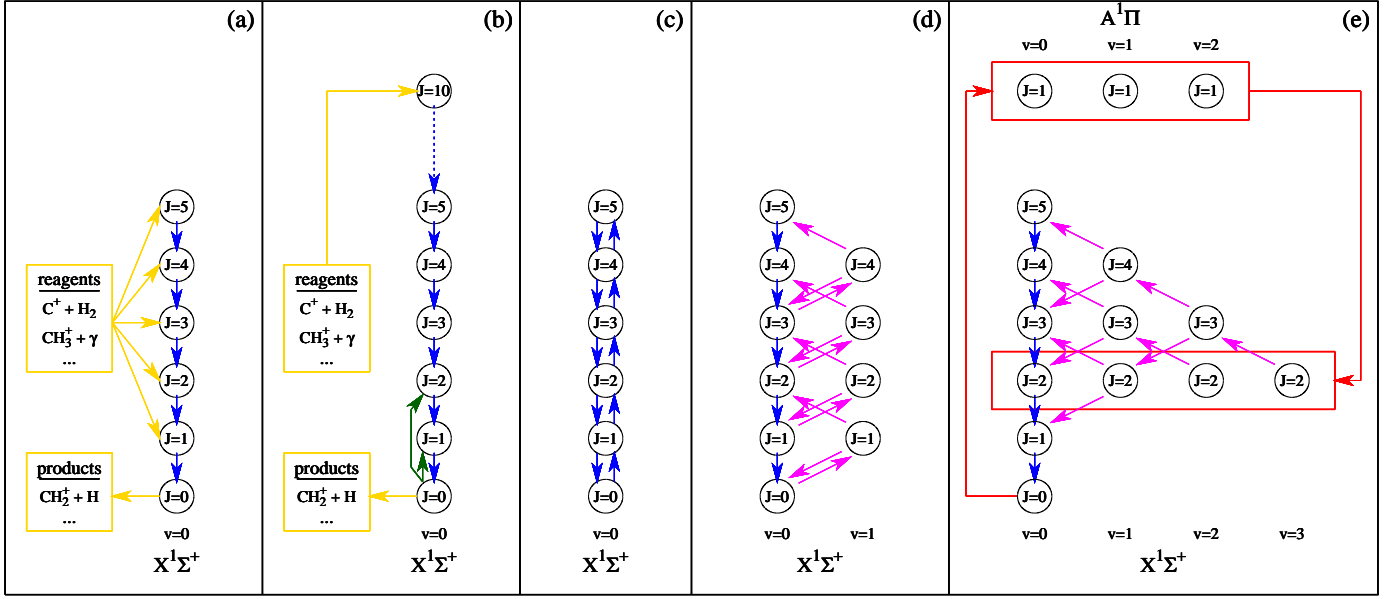


Figure B.1. Main excitation and de-excitation routes computed with MADEX, assuming $N(\text{CH}^+) = 10^{13} \text{ cm}^{-2}$, $u_{\text{exp}} = 1 \text{ km s}^{-1}$, $n_{\text{H}} = 10^4 \text{ cm}^{-3}$, and (a) $T_{\text{K}} = 100 \text{ K}$, $\chi_{\text{fir}} = 1$, $\chi_{\text{nir}} = 1$, and $\chi_{\text{opt}} = 1$, (b) $T_{\text{K}} = 1000 \text{ K}$, $\chi_{\text{fir}} = 1$, $\chi_{\text{nir}} = 1$, and $\chi_{\text{opt}} = 1$, (c) $T_{\text{K}} = 100 \text{ K}$, $\chi_{\text{fir}} = 10^6$, $\chi_{\text{nir}} = 1$, and $\chi_{\text{opt}} = 1$, (d) $T_{\text{K}} = 100 \text{ K}$, $\chi_{\text{fir}} = 1$, $\chi_{\text{nir}} = 10^{10}$, and $\chi_{\text{opt}} = 1$, (e) $T_{\text{K}} = 100 \text{ K}$, $\chi_{\text{fir}} = 1$, $\chi_{\text{nir}} = 1$, and $\chi_{\text{opt}} = 10^6$. The photodissociation process was intentionally neglected to focus on the (de)excitation of the bound-bound rovibronic transitions. The pure rotational, rovibrational, and rovibronic transitions are displayed in blue, purple, and red. Nonreactive and reactive collisional processes are displayed in green and yellow. In each case, the levels that do not contribute to the excitation of the pure rotational levels are not displayed (e.g. $\Lambda, \nu, J = 0, 1, 0$ in the case (d)). For more clarity the rotational emission lines from $J = 10$ to $J = 5$ are merged into a single dotted arrow in case (b), and all vibronic $\Lambda, J = 1, 1 \leftarrow 0, 0$ absorption lines and $\Lambda, J = 1, 1 \rightarrow 0, 2$ emission lines are merged into two single arrows in case (e).

more than 70 percent of the total destruction and formation rates are displayed.

In all cases the de-excitation of the rotational levels occurs via pure rotational transitions, as expected from the analytical treatment presented in appendix A. Conversely, four different excitation regimes are revealed: (a) by reactive collisions for all $J \geq 1$ levels, (b) by chemical pumping of a high-energy level (e.g. $J = 10$) followed by the cascade through the intermediate J levels, (c) by absorption of far-infrared photons by the $J-1$ level, (d) by near-infrared pumping of the $\Lambda, \nu = 0, 1$ levels, and (e) by optical pumping of the $\Lambda, J = 1, 1$ levels followed by the cascade through the vibrational levels of the $X^1\Sigma^+$ state. Using Eq. A.1 and taking into account all routes displayed in Fig. B.1, we derive at the steady-state equilibrium

$$\frac{n_{00J}}{n(\text{CH}^+)} = n_{\text{H}} \frac{([\text{H}] k_{\text{H}}^D + [\text{H}_2] k_{\text{H}_2}^D + [e^-] k_e^D)}{A_{00J00(J-1)}} \times \frac{(2J+1) \exp(-E_{00J}/T_{\text{K}})}{\sum_i (2i+1) \exp(-E_i/T_{\text{K}})} \quad (\text{B.1})$$

for $J \geq 1$ in case (a),

$$\frac{n_{00J}}{n(\text{CH}^+)} = n_{\text{H}} \frac{([\text{H}] k_{\text{H}}^D + [\text{H}_2] k_{\text{H}_2}^D + [e^-] k_e^D)}{A_{00J00(J-1)}} \times \frac{\max_{i>J} [(2i+1) \exp(-E_i/T_{\text{F}})]}{\sum_i (2i+1) \exp(-E_i/T_{\text{F}})} \quad (\text{B.2})$$

for $J \geq 3$ in case (b),

$$n_{00J} = n_{000} (2J+1) \chi_{\text{fir}}^J \prod_{i=1}^J \langle n_{\gamma, \nu_{i-1}} \rangle \quad (\text{B.3})$$

for $J \geq 2$ in case (c),

$$n_{00J} = n_{000} \chi_{\text{nir}}^{(J+1)/2} \left(\prod_{i=1}^{(J+1)/2} A_{00(2i-1)00(2i-2)} \right)^{-1} \times \left(\prod_{i=1}^{(J-1)/2} \frac{4i+1}{4i-1} \frac{\langle n_{\gamma, \nu} \rangle A_{01(2i)00(2i-1)}}{1 + \frac{A_{01(2i)00(2i-1)}}{A_{01(2i)00(2i+1)}}} \right) \left(3 \frac{\langle n_{\gamma, \nu} \rangle A_{011000}}{1 + \frac{A_{011000}}{A_{011002}}} \right) \quad (\text{B.4})$$

for odd J -values in case (d),

$$n_{00J} = n_{000} \chi_{\text{nir}}^{J/2} \left(\prod_{i=1}^{J/2} A_{00(2i)00(2i-1)} \right)^{-1} \times \left(\prod_{i=1}^{(J-2)/2} \frac{4i+3}{4i+1} \frac{\langle n_{\gamma, \nu} \rangle A_{01(2i+1)00(2i)}}{1 + \frac{A_{01(2i)00(2i-1)}}{A_{01(2i)00(2i+1)}}} \right) \left(3 \frac{\langle n_{\gamma, \nu} \rangle A_{011000}}{1 + \frac{A_{011000}}{A_{011002}}} \right) \quad (\text{B.5})$$

for even J -values in case (d), and

$$n_{00J} = n_{000} \frac{\chi_{\text{opt}}}{A_{00J00(J-1)}} \times \left(\sum_{\nu} 3 \langle n_{\gamma, \nu} \rangle A_{1\nu 1000} \frac{A_{1\nu 10(J-2)2}}{\sum_{\nu'} A_{1\nu 10\nu'0}} \right) \times \left(\prod_{i=3}^J \frac{1}{1 + \frac{A_{0(J-i+1)(i-1)0(J-i)2}}{A_{0(J-i+1)(i-1)0(J-i)i}}} \right) \quad (\text{B.6})$$

for $J \geq 2$ in case (e). In all these formulae, $\langle n_{\gamma, \nu} \rangle$ corresponds to the directionally averaged photon occupation number of the standard interstellar radiation field at the frequency ν of the radiative transitions.

Table 5. Predictions of MADEX applied to CH⁺ and SiO.

		^a CH ⁺					^b SiO						
	Λ	T_e (cm ⁻¹)	ω_e (cm ⁻¹)	B_e (cm ⁻¹)			T_e (cm ⁻¹)	ω_e (cm ⁻¹)	B_e (cm ⁻¹)				
	0		2.858 (+03)	1.418 (+01)				1.242 (+03)	7.242 (-01)				
	1	2.412 (+04)	1.864 (+03)	1.189 (+01)			4.284 (+04)	8.528 (+02)	6.307 (-01)				
		$M_{\Lambda'\nu'\Lambda''\nu''}$ (ea ₀)					$M_{\Lambda'\nu'\Lambda''\nu''}$ (ea ₀)						
	$\Lambda' \rightarrow \Lambda''$	$\nu'' \setminus \nu'$	0	1	2	3	4	0	1	2	3	4	
	0	0	2.2 (-1)	1.6 (-1)	1.0 (-1)	6.5 (-2)	4.1 (-2)	2.0 (+0)	2.7 (+0)	2.6 (+0)	2.0 (+0)	1.3 (+0)	
	1	1	1.1 (-1)	9.1 (-2)	1.5 (-1)	1.3 (-1)	1.1 (-1)	2.7 (+0)	1.9 (+0)	1.6 (+0)	1.5 (+0)	2.1 (+0)	
	2	2	4.6 (-2)	1.1 (-1)	1.6 (-2)	7.0 (-2)	1.0 (-1)	2.8 (+0)	1.4 (-1)	1.8 (+0)	1.5 (+0)	6.6 (-2)	
	3	3	1.6 (-2)	7.2 (-2)	6.5 (-2)	6.7 (-2)	1.5 (-2)	2.4 (+0)	1.3 (+0)	1.7 (+0)	3.4 (-1)	1.6 (+0)	
	4	4	5.1 (-3)	3.5 (-2)	7.6 (-2)	2.1 (-3)	5.2 (-2)	1.8 (+0)	2.1 (+0)	4.8 (-1)	1.6 (+0)	9.8 (-1)	
			$M_{\Lambda'\nu'\Lambda''\nu''}$ (ea ₀)					$M_{\Lambda'\nu'\Lambda''\nu''}$ (ea ₀)					
	0	0	6.6 (-1)	6.3 (-3)	6.6 (-5)	6.5 (-7)	6.5 (-9)	2.0 (+0)	4.1 (-2)	2.3 (-3)	1.6 (-4)	1.9 (-5)	
	1	1		6.6 (-1)	9.6 (-3)	7.7 (-4)	2.0 (-5)		6.1 (+0)	5.7 (-2)	4.4 (-3)	3.2 (-4)	
	2	2			6.7 (-1)	1.3 (-2)	2.9 (-3)			1.2 (+1)	6.9 (-2)	6.2 (-3)	
	3	3				6.7 (-1)	1.8 (-2)				1.8 (+1)	7.8 (-2)	
	4	4					6.8 (-1)					2.0 (+1)	
			$\sum [C]k_{J',J''}^C$ (cm ³ s ⁻¹)					$\sum [C]k_{J',J''}^C$ (cm ³ s ⁻¹)					
	$J'' \setminus J'$	0	1	2	3	4	5	0	1	2	3	4	5
	0		8.1 (-11)	5.3 (-11)	1.1 (-11)	8.4 (-12)	9.1 (-13)		2.8 (-11)	1.1 (-11)	7.3 (-12)	1.2 (-12)	2.1 (-12)
	1	1.6 (-10)		8.8 (-11)	7.5 (-11)	1.2 (-11)	1.9 (-11)	8.4 (-11)		4.9 (-11)	1.6 (-11)	1.4 (-11)	2.0 (-12)
	2	8.0 (-11)	6.6 (-11)		5.9 (-11)	8.4 (-11)	5.4 (-12)	5.0 (-11)	7.8 (-11)		5.4 (-11)	1.9 (-11)	1.7 (-11)
	3	7.0 (-12)	2.4 (-11)	2.5 (-11)		3.7 (-11)	7.1 (-11)	4.5 (-11)	3.4 (-11)	7.1 (-11)		5.5 (-11)	2.0 (-11)
	4	1.4 (-12)	9.5 (-13)	9.2 (-12)	9.6 (-12)		2.4 (-11)	8.5 (-12)	3.4 (-11)	2.9 (-11)	6.6 (-11)		5.6 (-11)
	5	2.5 (-14)	2.5 (-13)	9.8 (-14)	3.1 (-12)	4.0 (-12)		1.7 (-11)	5.5 (-12)	2.8 (-11)	2.6 (-11)	6.1 (-11)	
		$\sum [D]k^D$ (cm ³ s ⁻¹)	$\int \frac{4\pi}{h\nu} \sigma^\gamma(\nu) I_\nu d\nu$ (s ⁻¹)				$\sum [D]k^D$ (cm ³ s ⁻¹)	$\int \frac{4\pi}{h\nu} \sigma^\gamma(\nu) I_\nu d\nu$ (s ⁻¹)					
		6.24 (-10)	3.30 (-10)				9.35 (-14)	1.60 (-09)					
		$n_J/n(\text{CH}^+)$					$n_J/n(\text{SiO})$						
	J	0	1	2	3	4	5	0	1	2	3	4	5
	①	1.0 (+00)	1.4 (-03)	1.5 (-05)	3.8 (-07)	2.6 (-08)	3.2 (-10)	2.6 (-01)	4.5 (-01)	2.3 (-01)	4.2 (-02)	3.5 (-03)	3.1 (-04)
	②	1.0 (+00)	4.3 (-03)	5.9 (-05)	4.8 (-06)	4.5 (-07)	3.4 (-08)	2.6 (-01)	4.5 (-01)	2.3 (-01)	4.2 (-02)	3.5 (-03)	3.1 (-04)
	③	1.0 (+00)	4.3 (-03)	5.9 (-05)	4.8 (-06)	4.5 (-07)	3.4 (-08)	2.6 (-01)	4.5 (-01)	2.3 (-01)	4.2 (-02)	3.5 (-03)	3.1 (-04)
χ_{nir}	10 ³	1.0 (+00)	4.3 (-03)	5.9 (-05)	4.8 (-06)	4.5 (-07)	3.4 (-08)	2.6 (-01)	4.5 (-01)	2.3 (-01)	4.2 (-02)	3.6 (-03)	3.1 (-04)
	10 ⁵	1.0 (+00)	4.3 (-03)	5.9 (-05)	4.8 (-06)	4.5 (-07)	3.4 (-08)	2.1 (-01)	4.2 (-01)	2.8 (-01)	7.1 (-02)	7.2 (-03)	5.4 (-04)
	10 ⁷	1.0 (+00)	4.6 (-03)	7.0 (-05)	4.8 (-06)	4.5 (-07)	3.4 (-08)	2.5 (-01)	4.5 (-01)	2.3 (-01)	4.5 (-02)	4.0 (-03)	3.7 (-04)
$\chi_{\text{opt/UV}}$	10 ²	1.0 (+00)	4.3 (-03)	6.1 (-05)	4.9 (-06)	4.5 (-07)	3.4 (-08)	2.1 (-01)	4.3 (-01)	2.6 (-01)	7.1 (-02)	9.3 (-03)	1.1 (-03)
	10 ³	9.9 (-01)	5.0 (-03)	7.2 (-05)	5.4 (-06)	4.8 (-07)	3.6 (-08)	9.3 (-02)	3.0 (-01)	3.1 (-01)	1.9 (-01)	7.1 (-02)	1.8 (-02)
	10 ⁴	1.0 (+00)	4.3 (-03)	6.0 (-05)	4.8 (-06)	4.5 (-07)	3.4 (-08)	2.5 (-01)	4.5 (-01)	2.3 (-01)	4.8 (-02)	4.5 (-03)	4.8 (-04)
	10 ³	1.0 (+00)	4.5 (-03)	6.3 (-05)	5.1 (-06)	4.7 (-07)	3.6 (-08)	1.9 (-01)	4.1 (-01)	2.8 (-01)	9.0 (-02)	1.5 (-02)	2.4 (-03)
	10 ⁴	9.9 (-01)	6.4 (-03)	9.9 (-05)	8.0 (-06)	7.2 (-07)	5.5 (-08)	6.6 (-02)	2.5 (-01)	2.9 (-01)	2.2 (-01)	1.1 (-01)	3.8 (-02)

From top to bottom: molecular constants of the X¹Σ⁺ and A¹Π electronic states, transition dipole moments of the A¹Π – X¹Σ⁺ and X¹Σ⁺ – X¹Σ⁺ band systems, nonreactive collisional rates, chemical destruction rates and photodissociation rates, and populations of the rotational levels predicted with MADEX for $J \leq 5$. The collisional rates and the predictions of the level populations are computed for $T_D = T_F = T_K = 100$ K, $n_H = 10^4$ cm⁻³, $[\text{H}_2] = 0.5$, and $[e^-] = 10^{-4}$. For both molecules, MADEX was run in the four configurations ①, ②, ③, and ④ (see main text). In cases ③ and ④, the values of the radiation field scaling factors χ_{nir} and $\chi_{\text{opt/UV}}$ are 1 unless specified otherwise. Numbers in parenthesis are power of ten.

^a data from Hakalla et al. (2006); Cheng et al. (2007); Lim et al. (1999); Hammami et al. (2008); Turpin et al. (2010); ^bdata from Hedelund & Lambert (1972); Beer et al. (1974); Barrow & Stone (1975); Elander & Smith (1973); Naidu (1981); Drira et al. (1997); Tipping & Chackerian (1981); Liszt & Smith (1972); Drira et al. (1998); Park et al. (1993); Dayou & Balança (2006)

Table 6. Same as Table 5 for HF and CS.

		^a HF					^b CS						
Λ		T_e (cm ⁻¹)	ω_e (cm ⁻¹)	B_e (cm ⁻¹)			T_e (cm ⁻¹)	ω_e (cm ⁻¹)	B_e (cm ⁻¹)				
0			4.138 (+03)	2.056 (+01)				1.285 (+03)	8.200 (-01)				
1							3.890 (+04)	1.073 (+03)	7.800 (-01)				
		$M_{\Lambda',v',\Lambda'',v''} (ea_0)$					$M_{\Lambda',v',\Lambda'',v''} (ea_0)$						
$v'' \setminus v'$		0	1	2	3	4	0	1	2	3	4		
$\Lambda' \rightarrow \Lambda''$	0						2.0 (-1)	9.2 (-2)	2.9 (-2)	6.6 (-3)			
	1						6.4 (-2)	1.6 (-1)	1.2 (-1)	5.2 (-2)	3.6 (-2)		
	2						1.9 (-2)	8.3 (-2)	1.2 (-1)	1.3 (-1)	2.2 (-1)		
	3						4.8 (-3)	3.3 (-2)	9.1 (-2)	8.3 (-2)	4.7 (-1)		
	4						7.8 (-3)	6.2 (-2)	2.4 (-1)	4.2 (-1)	1.3 (-1)		
		$M_{\Lambda',v',\Lambda'',v''} (ea_0)$					$M_{\Lambda',v',\Lambda'',v''} (ea_0)$						
$v'' \setminus v'$		0	1	2	3	4	0	1	2	3	4		
$\Lambda' \rightarrow \Lambda''$	0	7.2 (-1)	3.6 (-2)	4.5 (-3)	5.6 (-4)	8.2 (-5)	7.7 (-1)	6.2 (-2)	3.6 (-3)	2.4 (-4)	2.0 (-5)		
	1		7.3 (-1)	4.7 (-2)	7.5 (-3)	1.1 (-3)		7.6 (-1)	8.8 (-2)	6.3 (-2)	2.0 (-3)		
	2			7.5 (-1)	5.3 (-2)	1.0 (-2)			7.4 (-1)	3.9 (-2)	1.2 (-2)		
	3				7.7 (-1)	5.6 (-2)				7.3 (-1)	3.9 (-2)		
	4					7.8 (-1)					7.1 (-1)		
		$\sum [C] k_{J',J''}^C (\text{cm}^3 \text{s}^{-1})$					$\sum [C] k_{J',J''}^C (\text{cm}^3 \text{s}^{-1})$						
$J'' \setminus J'$		0	1	2	3	4	5	0	1	2	3	4	5
0			7.0 (-11)	3.3 (-12)	7.9 (-13)	1.8 (-13)	9.7 (-14)		1.7 (-11)	1.9 (-11)	3.1 (-12)	2.9 (-12)	7.5 (-13)
1		1.2 (-10)		4.9 (-11)	1.4 (-12)	2.8 (-12)	9.6 (-14)	4.9 (-11)		2.5 (-11)	2.9 (-11)	5.3 (-12)	5.4 (-12)
2		2.7 (-12)	2.5 (-11)		2.4 (-11)	8.7 (-13)	2.9 (-12)	8.6 (-11)	4.0 (-11)		2.6 (-11)	3.2 (-11)	6.5 (-12)
3		1.5 (-13)	1.6 (-13)	5.4 (-12)		1.3 (-11)	2.1 (-11)	1.9 (-11)	5.9 (-11)	3.4 (-11)		2.8 (-11)	3.2 (-11)
4		3.8 (-15)	3.7 (-14)	2.3 (-14)	1.5 (-12)		8.6 (-12)	2.1 (-11)	1.3 (-11)	4.8 (-11)	3.3 (-11)		2.6 (-11)
5		1.3 (-16)	7.6 (-17)	4.6 (-15)	1.4 (-13)	5.1 (-13)		5.8 (-12)	1.4 (-11)	1.1 (-11)	4.0 (-11)	2.8 (-11)	
		$\sum [D] k^D (\text{cm}^3 \text{s}^{-1})$					$\sum [D] k^D (\text{cm}^3 \text{s}^{-1})$						
		8.42 (-13)					1.16 (-14)						
		$\int \frac{4\pi}{h\nu} \sigma^\gamma(\nu) I_\nu d\nu (\text{s}^{-1})$					$\int \frac{4\pi}{h\nu} \sigma^\gamma(\nu) I_\nu d\nu (\text{s}^{-1})$						
		1.17 (-10)					9.80 (-10)						
		$n_J/n(\text{HF})$					$n_J/n(\text{CS})$						
J		0	1	2	3	4	5	0	1	2	3	4	5
①		1.0 (+00)	2.0 (-04)	1.2 (-07)	1.7 (-09)	1.8 (-11)	2.9 (-13)	2.5 (-01)	4.8 (-01)	2.2 (-01)	3.9 (-02)	5.3 (-03)	1.2 (-03)
②		1.0 (+00)	2.0 (-04)	1.3 (-07)	2.3 (-09)	4.3 (-11)	1.0 (-12)	2.5 (-01)	4.8 (-01)	2.2 (-01)	3.9 (-02)	5.3 (-03)	1.2 (-03)
10 ³ ③		1.0 (+00)	2.0 (-04)	1.5 (-07)	2.4 (-09)	4.3 (-11)	1.0 (-12)	2.5 (-01)	4.8 (-01)	2.2 (-01)	3.9 (-02)	5.3 (-03)	1.2 (-03)
10 ⁵ ④		1.0 (+00)	2.8 (-04)	2.1 (-06)	1.1 (-08)	5.9 (-11)	1.0 (-12)	2.5 (-01)	4.8 (-01)	2.2 (-01)	4.1 (-02)	5.4 (-03)	1.2 (-03)
10 ⁷ ⑤		9.9 (-01)	8.2 (-03)	2.0 (-04)	1.1 (-06)	5.3 (-09)	2.5 (-11)	1.3 (-01)	3.9 (-01)	3.2 (-01)	1.2 (-01)	2.5 (-02)	4.0 (-03)
10 ² ⑥								2.5 (-01)	4.8 (-01)	2.2 (-01)	3.9 (-02)	5.3 (-03)	1.2 (-03)
10 ³ ⑦								2.5 (-01)	4.8 (-01)	2.2 (-01)	4.0 (-02)	5.3 (-03)	1.2 (-03)
10 ⁴ ⑧								2.4 (-01)	4.7 (-01)	2.3 (-01)	4.3 (-02)	5.8 (-03)	1.2 (-03)
10 ² ⑨		1.0 (+00)	2.0 (-04)	1.4 (-07)	3.0 (-09)	7.6 (-11)	2.0 (-12)	2.5 (-01)	4.7 (-01)	2.2 (-01)	4.2 (-02)	6.0 (-03)	1.5 (-03)
10 ³ ⑩		1.0 (+00)	2.1 (-04)	2.6 (-07)	9.9 (-09)	3.8 (-10)	1.1 (-11)	2.1 (-01)	4.5 (-01)	2.5 (-01)	6.2 (-02)	1.3 (-02)	4.2 (-03)
10 ⁴ ⑪		1.0 (+00)	3.4 (-04)	1.5 (-06)	7.8 (-08)	3.4 (-09)	9.9 (-11)	6.8 (-02)	2.9 (-01)	3.2 (-01)	1.8 (-01)	7.2 (-02)	3.0 (-02)

^a data from Webb & Narahari Rao (1968); Johns & Barrow (1959); Meredith (1973); Reese et al. (2005); Guillon & Stoecklin (2012); ^b data from Lovas & Krupenie (1974); Winnewisser & Cook (1968); Botschwina & Sebald (1985); Turner et al. (1992); Lique & Spielfiedel (2007)

Table 7. Same as Table 5 for HCl and CO. In contrast to other molecules, the $\Lambda = 1$ state of HCl corresponds to its $C^1\Pi$ (and not $A^1\Pi$) electronic configuration.

		^a HCl					^b CO						
Λ		T_e (cm ⁻¹)	ω_e (cm ⁻¹)	B_e (cm ⁻¹)			T_e (cm ⁻¹)	ω_e (cm ⁻¹)	B_e (cm ⁻¹)				
0			2.990 (+03)	1.059 (+01)				2.170 (+03)	1.931 (+00)				
1		7.758 (+04)	2.684 (+03)	9.330 (+00)			6.508 (+04)	1.518 (+03)	1.612 (+00)				
		$M_{\Lambda'v'\Lambda''v''}$ (ea ₀)					$M_{\Lambda'v'\Lambda''v''}$ (ea ₀)						
$v''\backslash v'$		0	1	2	3	4	0	1	2	3	4		
$\Lambda' \rightarrow \Lambda''$	0	8.6 (-1)					2.9 (-1)	4.0 (-1)	4.2 (-1)	3.8 (-1)	3.0 (-1)		
	1	5.8 (-1)					4.2 (-1)	3.3 (-1)	9.1 (-2)	1.2 (-1)	2.3 (-1)		
	2	4.2 (-1)					4.2 (-1)	4.2 (-2)	2.5 (-1)	2.9 (-1)	1.7 (-1)		
	3	1.9 (-1)					3.3 (-1)	2.2 (-1)	2.7 (-1)	2.5 (-2)	1.8 (-1)		
	4	1.3 (-1)					2.2 (-1)	3.3 (-1)	4.9 (-2)	2.4 (-1)	2.2 (-1)		
		$M_{\Lambda'v'\Lambda''v''}$ (ea ₀)					$M_{\Lambda'v'\Lambda''v''}$ (ea ₀)						
$v''\backslash v'$		0	1	2	3	4	0	1	2	3	4		
$\Lambda' \rightarrow \Lambda''$	0	4.3 (-1)	2.8 (-2)	3.1 (-3)	2.2 (-4)	1.2 (-5)	4.3 (-2)	4.1 (-2)	2.6 (-3)	1.6 (-4)	8.1 (-6)		
	1		4.9 (-1)	2.0 (-2)	2.0 (-3)	2.0 (-4)		3.3 (-2)	5.7 (-2)	4.4 (-3)	3.4 (-4)		
	2			6.0 (-3)	2.0 (-2)	2.0 (-3)			2.4 (-2)	4.0 (-2)	3.6 (-3)		
	3				6.1 (-1)	2.0 (-2)				1.4 (-2)	4.5 (-2)		
	4					3.4 (-1)					3.8 (-3)		
		$\sum [C]k_{J',J''}^C$ (cm ³ s ⁻¹)					$\sum [C]k_{J',J''}^C$ (cm ³ s ⁻¹)						
$J''\backslash J'$		0	1	2	3	4	5	0	1	2	3	4	5
0			7.9 (-12)	3.0 (-12)	2.3 (-12)	1.3 (-12)	4.5 (-13)		2.1 (-11)	2.8 (-11)	7.8 (-12)	3.8 (-12)	2.3 (-12)
1			1.7 (-11)	2.0 (-11)	7.0 (-12)	2.4 (-12)	1.3 (-12)	6.1 (-11)		4.1 (-11)	4.0 (-11)	1.5 (-11)	6.4 (-12)
2			6.1 (-12)	1.8 (-11)	2.3 (-11)	7.2 (-12)	1.5 (-12)	1.2 (-10)	6.1 (-11)		4.6 (-11)	4.3 (-11)	1.7 (-11)
3			2.6 (-12)	3.5 (-12)	1.3 (-11)	2.6 (-11)	6.9 (-12)	3.9 (-11)	7.2 (-11)		5.5 (-11)	4.7 (-11)	4.5 (-11)
4			5.4 (-13)	4.6 (-13)	1.5 (-12)	9.8 (-12)	2.6 (-11)	2.0 (-11)	2.7 (-11)	5.3 (-11)	4.9 (-11)		4.8 (-11)
5			5.1 (-14)	6.9 (-14)	8.3 (-14)	7.0 (-13)	6.8 (-12)	1.1 (-11)	1.1 (-11)	2.0 (-11)	4.3 (-11)	4.5 (-11)	
		$\sum [D]k^D$ (cm ³ s ⁻¹)					$\sum [D]k^D$ (cm ³ s ⁻¹)						
		2.29 (-13)					2.28 (-17)						
		$\int \frac{4\pi}{h\nu} \sigma^\gamma(\nu) I_\nu d\nu$ (s ⁻¹)					$\int \frac{4\pi}{h\nu} \sigma^\gamma(\nu) I_\nu d\nu$ (s ⁻¹)						
		9.80 (-10)					2.60 (-10)						
		$n_J/n(\text{HCl})$					$n_J/n(\text{CO})$						
J		0	1	2	3	4	5	0	1	2	3	4	5
10 ³ ①		1.0 (+00)	4.9 (-04)	8.5 (-06)	8.1 (-07)	6.1 (-08)	2.7 (-09)	7.3 (-02)	2.5 (-01)	3.3 (-01)	2.2 (-01)	8.9 (-02)	2.9 (-02)
10 ⁵ ②		1.0 (+00)	4.9 (-04)	8.6 (-06)	8.2 (-07)	6.3 (-08)	2.9 (-09)	7.3 (-02)	2.5 (-01)	3.3 (-01)	2.2 (-01)	8.9 (-02)	2.9 (-02)
10 ⁷ ③		1.0 (+00)	4.9 (-04)	8.7 (-06)	8.2 (-07)	6.3 (-08)	2.9 (-09)	7.3 (-02)	2.5 (-01)	3.3 (-01)	2.2 (-01)	8.9 (-02)	2.9 (-02)
10 ² ④		1.0 (+00)	7.5 (-04)	2.3 (-05)	8.9 (-07)	6.3 (-08)	2.9 (-09)	7.1 (-02)	2.4 (-01)	3.3 (-01)	2.2 (-01)	9.4 (-02)	3.1 (-02)
10 ³ ⑤		9.7 (-01)	2.6 (-02)	1.4 (-03)	1.3 (-05)	2.2 (-07)	4.3 (-09)	3.3 (-02)	9.8 (-02)	1.6 (-01)	2.0 (-01)	2.0 (-01)	1.5 (-01)
10 ⁴ ⑥		1.0 (+00)	5.0 (-04)	9.0 (-06)	8.5 (-07)	6.4 (-08)	3.0 (-09)	7.3 (-02)	2.5 (-01)	3.3 (-01)	2.2 (-01)	9.0 (-02)	3.0 (-02)
10 ⁵ ⑦		1.0 (+00)	6.1 (-04)	1.3 (-05)	1.0 (-06)	7.7 (-08)	3.4 (-09)	7.0 (-02)	2.3 (-01)	3.3 (-01)	2.3 (-01)	9.8 (-02)	3.3 (-02)
10 ⁶ ⑧		1.0 (+00)	1.7 (-03)	4.8 (-05)	3.1 (-06)	2.1 (-07)	8.4 (-09)	5.3 (-02)	1.7 (-01)	2.6 (-01)	2.6 (-01)	1.6 (-01)	7.0 (-02)
10 ² ⑨		1.0 (+00)	6.5 (-04)	1.4 (-05)	1.5 (-06)	1.5 (-07)	1.4 (-08)	7.2 (-02)	2.4 (-01)	3.3 (-01)	2.2 (-01)	9.2 (-02)	3.1 (-02)
10 ³ ⑩		1.0 (+00)	2.1 (-03)	6.3 (-05)	7.4 (-06)	9.4 (-07)	1.1 (-07)	6.3 (-02)	2.1 (-01)	3.1 (-01)	2.3 (-01)	1.1 (-01)	4.2 (-02)
10 ⁴ ⑪		9.8 (-01)	1.6 (-02)	5.6 (-04)	6.7 (-05)	8.9 (-06)	1.1 (-06)	3.7 (-02)	1.2 (-01)	2.0 (-01)	2.4 (-01)	1.9 (-01)	1.2 (-01)

^a data from Rank et al. (1965); Tilford et al. (1970); van Dishoeck et al. (1982); Li et al. (2011); Neufeld & Green (1994);^b data from Macris & Petropoulos (1985); Eidelsberg et al. (1992); Chantranupong (1992); Sundholm et al. (1995); Goorvitch (1994); Kiriyama & Rao (2001); Flower (2001)